

The Arecibo Legacy Fast ALFA Survey VII: A Neutral Hydrogen Cloud Complex in the Virgo Cluster

Brian R. Kent^{1,2}, Kristine Spekkens³, Riccardo Giovanelli^{4,5}, Martha P. Haynes^{4,5},
Emmanuel Momjian⁶, Juan R. Cortés^{7,8}, Eduardo Hardy^{9,7}, and Andrew A. West¹⁰

Received _____; accepted _____

¹Jansky Fellow of the National Radio Astronomy Observatory.

²National Radio Astronomy Observatory, 520 Edgemont Road, Charlottesville, VA 22903.
The National Radio Astronomy Observatory is a facility of the National Science Foundation operated under cooperative agreement by Associated Universities, Inc. *e-mail*: bkent@nrao.edu

³Department of Physics, Royal Military College of Canada, P.O. Box 17000, Station Forces, Kingston, Ontario, K7K 7B4. *e-mail*: Kristine.Spekkens@rmc.ca

⁴Center for Radiophysics and Space Research, Space Sciences Building, Cornell University, Ithaca, NY 14853. *e-mail*: riccardo@astro.cornell.edu, haynes@astro.cornell.edu

⁵National Astronomy and Ionosphere Center, Cornell University, Space Sciences Building, Ithaca, NY 14853. The National Astronomy and Ionosphere Center is operated by Cornell University under a cooperative agreement with the National Science Foundation.

⁶National Radio Astronomy Observatory, 1003 Lopezville Rd., P. O. Box O, Socorro, NM 87801. *e-mail*: emomjian@nrao.edu

⁷Departamento de Astronomía, Universidad de Chile, Casilla 36-D, Santiago, Chile *e-mail*: jcortes@das.uchile.cl

⁸National Astronomical Observatory of Japan, 2-21-1 Osawa, Mitaka, Tokyo, 181-8588

⁹National Radio Astronomy Observatory, Casilla El Golf 16-10, Las Condes, Santiago, Chile *e-mail*: ehardy@nrao.edu

¹⁰Astronomy Department, 601 Campbell Hall, University of California, Berkeley, CA 94720-3411 *e-mail*: awest@astro.berkeley.edu

ABSTRACT

We present observations of an HI cloud complex most likely located in the Virgo galaxy cluster, first reported by Kent *et al.* (2007). The complex consists of five clouds, detected in the data set of the ALFALFA extragalactic HI survey at Arecibo. The clouds have radial velocities between $cz_{\odot} \sim 480$ and 610 km s^{-1} . At the Virgo cluster distance, they are spread over a projected span of 170 kpc and have HI masses ranging from 0.48 to $1.7 \times 10^8 M_{\odot}$. The overall HI mass of the complex is $5.1 \times 10^8 M_{\odot}$. The clouds’ velocity widths vary between 50 and 250 km s^{-1} . New results of follow-up aperture synthesis observations conducted with the Very Large Array are also presented, which yield a higher resolution view of two of the clouds in the complex. These two resolved clouds show no evidence of symmetry in the gas distribution or of any ordered motions. The possibility that the complex is a group of primordial objects, embedded in their own dark matter halo is thought to be unlikely. Scenarios in which the clouds have been removed from the disk of a galaxy traveling at high speed through the intracluster medium are considered. The most likely among those is thought to be one where the clouds were separated from NGC 4445 at a time $> 0.5 \text{ Gyr}$ ago. The orbital velocity of the clouds and the putative parent galaxy would now be seen at a relatively large angle with respect to the line of sight.

Subject headings: galaxies: intergalactic medium — galaxies: halos — radio lines: galaxies — galaxies:clusters — galaxies: interactions galaxies: individual (NGC 4445, NGC 4424)

1. Introduction

The study of the cold gas content in extragalactic systems plays an important role in understanding their formation and evolution. Not only does the gas content reveal information on the star formation potential of a galaxy, it can also help trace the dynamic history and response to the surrounding environment, whether it inhabits a dense cluster or an unpopulated field. For example, the fingerprint of galactic collisions and ram pressure stripping effects can be seen in the form of detached gaseous fragments and clumps. The 21 cm spectral line of neutral hydrogen serves as an important tool for measuring the cool, neutral gas component of galaxies, as well as a redshift indicator and kinematical probe. The HI line can also be detected in low mass systems with little or no stellar emission. Blind HI surveys thus yield samples which include a population “underappreciated” in optical surveys.

A number of intergalactic HI clouds have been reported in the literature, some in pairs and groups or in the vicinity of large disk galaxies (e.g. Schneider *et al.* 1983; Sancisi *et al.* 1987; Kilborn *et al.* 2000; Ryder *et al.* 2001), others the result of disturbances from interactions within a cluster (Minchin *et al.* 2005, 2007; Oosterloo & van Gorkom 2005; Haynes *et al.* 2007). The serendipitous detection of HI1225+01 (Giovanelli & Haynes 1989; Chengalur *et al.* 1995) revealed a binary structure, with the NE component found to be associated with a dwarf galaxy, while the SW component has failed to yield any optical light down to a surface magnitude limit of 27 mag arcsec⁻² (Salzer *et al.* 1991). A recently reported HI feature, VirgoHI21, was detected north of the spiral galaxy NGC 4254 (Minchin *et al.* 2005) and interpreted as a fairly massive “dark galaxy”. ALFALFA survey data, which provides full coverage of the region, indicate that VirgoHI21 is not an isolated dark galaxy, but rather a tidal tail of NGC 4254 resulting from the high speed encounter of that galaxy with a now distant interloper (Haynes *et al.* 2007; Duc & Bournaud 2008).

A galaxy traveling through a cluster can be affected by a variety of mechanisms, the

most commonly invoked being ram pressure stripping. The study of HI deficiency in Virgo spirals was pioneered by Davies & Lewis (1973), with the first reliably measured deficiencies reported by Chamaraux, Balkowski & Gerard (1980). Giovanelli & Haynes (1983) showed that HI deficient galaxies in Virgo had truncated HI disks. These results were extended to other clusters (Giovanelli & Haynes 1985; Haynes & Giovanelli 1986; Haynes, Giovanelli & Chincarini 1984) and mapped with higher resolution (Cayatte *et al.* 1990; Chung *et al.* 2007). Oosterloo & van Gorkhom (2005) recently reported the discovery of a HI cloud in the vicinity of the Virgo spiral NGC 4388 with a HI mass of $3.4 \times 10^8 M_{\odot}$, resolved into distinct clumps. They show a clear connection to NGC 4388. It has also been shown that galaxies can be “harassed” by the collective effect of the cluster potential and multiple high speed encounters with other cluster members (e.g. Moore *et al.* 1996; Mihos *et al.* 2005). The hot intracluster gas is a hostile environment for the cold material removed from cluster galaxies through these processes. The interaction remnants represented by the latter are thus transient features. A full census of their number and estimates of longevity can provide insights on the metal enrichment of the intracluster gas.

Virgo is the nearest rich cluster of galaxies, thus providing the best target for the detailed study of many environment driven effects on the evolution of galaxies. With over 1300 cataloged detections (Binggeli *et al.* 1985), the overdensity associated with the Virgo cluster extends over more than 300 square degrees in the sky, distributed in several subclumps. The largest two clumps are centered around large elliptical galaxies, M87 for the main clump, and M49 for the southern subclump. The morphology–density relation is well established in the cluster, with late type objects thought to be still falling into the cluster, as it dynamically evolves. The dynamically vulnerable, extended HI disks of late type galaxies can be easy victims of the processes discussed above. Optical data bases, such as the Digital Sky Survey (Lasker *et al.* 1990) and the Sloan Digital Sky Survey (York *et al.* 2000), provide photometry and targeted spectroscopy of cluster objects, as does the compendium of Virgo galaxies data of GOLDMINE website (<http://goldmine.mib.infn.it/>)

; Gavazzi *et al.* 2003). Individual galaxy distances are growing in number thanks to the ACS Virgo Cluster survey, which focuses on early-type galaxies via the surface-brightness fluctuation method (Mei *et al.* 2007). Targeted HI surveys also have played an important role in the overall characterization of the cluster (see, e.g. GOLDMINE for references).

The HI Parkes All-Sky Survey (HIPASS; Barnes *et al.* 2001) has mapped 30000 deg², part of which covers Virgo in the region $12^h < \text{R.A.} < 13^h$ and $+2^\circ < \text{Dec.} < +20^\circ$. HIPASS catalogs available from NED list 125 galaxies in this region. The Arecibo Legacy Fast ALFA Survey (ALFALFA; Giovanelli *et al.* 2005) is more sensitive and has significantly higher angular and spectral resolution than HIPASS. It is thus providing a much more incisive look into the HI properties of the cluster. While the HI content of many individual spiral galaxies has been mapped in detail with interferometry (Cayatte *et al.* 1990, 1994; Chung *et al.* 2007), no survey has covered the Virgo cluster region with the sensitivity and completeness of ALFALFA. It is a primary goal of the ALFALFA survey to study and characterize the local HI Universe, including the Virgo cluster. ALFALFA will provide a fair, well-sampled and homogeneous spectral dataset, covering 7000 deg² of the high galactic latitude sky out to a redshift of $cz_\odot \sim 18000 \text{ km s}^{-1}$. Approximately 250 deg² of the Virgo cluster in the range $11^h44^m < \text{R.A. (J2000)} < 14^h00^m$ and $+8^\circ < \text{Dec. (J2000)} < +16^\circ$ have been completely surveyed as of late 2007, with catalogs of extracted source parameters already released for publication (Giovanelli *et al.* 2007; Kent *et al.* 2008). A key feature of the survey is its sensitivity to low HI mass objects – ALFALFA will provide a complete HI census down to $2 \times 10^7 M_\odot$ at the Virgo distance. Sampling the low-mass population will be key in determining the HI mass function in the cluster environment, as well as in the field. The ALFALFA dataset in Virgo has already yielded many new interesting results (Kent *et al.* 2007; Haynes *et al.* 2007; Koopmann *et al.* 2008).

In this paper we give a detailed description of a multi-component HI cloud complex in the Virgo cluster region initially reported by Kent *et al.* (2007). In section 2 we describe the observations and data reduction method within the context of ALFALFA and the

cloud detections made with that dataset. In section 3 we detail follow-up observations conducted with the Very Large Array. In section 4 we discuss CO observations of the cloud. Section 5 discusses the environment of the cloud complex. Section 6 discusses possible formation mechanisms for the cloud complex. Section 7 summarizes the results of the paper. Throughout the paper we assume a distance to the Virgo Cluster of $D_V=16.7$ Mpc, and refer to the heliocentric reference frame for all velocities.

2. Discovery of a HI Cloud Complex

The ALFALFA observing strategy is described in detail by Giovanelli *et al.* (2005). The data are obtained in a meridian transit drift mode with the Arecibo L -band Feed Array (ALFA). Raw scans consist of 14 spectra ($7 \text{ beams} \times 2 \text{ linear polarizations/beam}$), sampled at a rate of 1 Hz. The spectra span a 100 MHz bandwidth with 4096 channels per polarization, centered at 1385 MHz. The resulting spectral resolution is 24.4 kHz before smoothing, corresponding to $\delta V = 5.1 \text{ km s}^{-1}$ at the rest frequency of the 21cm HI line. Scans are calibrated, baselined, and flagged for radio frequency interference, and then combined into regularly sampled data cubes.

Details of the ALFALFA data processing can be found in Kent (2008, PhD thesis). Briefly, frequency channels in each grid have been baselined with linear fits and then “flatfielded”, where a median subtraction has been performed in both the right ascension and declination directions. A matched-filter algorithm was used for signal detection, with manual follow-up (Saintonge 2007). The careful attention to signal extraction, analysis, and data quality has proven to be invaluable in detecting faint objects and optimizing the output of the signal extraction process.

The cloud complex was discovered in the ALFALFA data obtained in the Spring 2005 campaign, which sampled the Virgo core region ($12^{\text{h}} < \alpha < 13^{\text{h}}, 8^{\circ} < \delta < 16^{\circ}$). The data presented here are taken from a $2^{\circ}.4 \times 2^{\circ}.4$ data cube centered at $\alpha = 12^{\text{h}}20^{\text{m}}, \delta = 9^{\circ}00'$

(J2000). The system temperatures of the ALFA receivers during the observations were in the range $26 \text{ K} < T_{\text{sys}} < 30 \text{ K}$, yielding a root mean square (rms) noise of $\sigma_m = 2.5 \text{ mJy/beam}$ in channels with $\delta V = 5.1 \text{ km s}^{-1}$. The characteristics of the ALFALFA data cube from which the data are taken are summarized in Table 1.

2.1. ALFALFA Observations

The cloud complex is located near $\alpha \sim 12^{\text{h}}30^{\text{m}}, \delta \sim 9^{\circ}30'$ – this places it 2.9° (845 kpc in projection) South of M87 and 1.5° (432 kpc in projection) north of M49. We discuss the optical environment of the cloud complex in Section 5.

The complex consists of five distinct emission features or “clouds”, which we denote C1–C5. Together, they span approximately $35'$ (170 kpc in projection at the cluster distance) on the sky and 130 km s^{-1} in velocity. Channel maps of the ALFALFA dataset in the vicinity of these detections are shown in Figure 1, and total intensity (zeroth moment) and intensity-weighted velocity maps of the region is in Figure 2. An integrated spectral profile for each cloud is presented in Figure 3.

The individual properties of the clouds derived from the ALFALFA data are given in Table 2; all parameters are computed in the manner described by Giovanelli *et al.* (2007). The spatial centroid of each cloud is in col. (2). Its accuracy depends on the source strength, and varies from an average of $\sim 15''$ for the brightest features to $\sim 30''$ for the faintest ones. The heliocentric velocity cz_{\odot} , width at 50% of the peak W_{50} and total flux F_c of the integrated spectral profiles in Figure 3 are in cols. (3)–(5). The signal-to-noise ratio S/N of the detections is in col. (6), and is given by

$$S/N = \left(\frac{1000 F_c}{W_{50}} \right) \frac{w_{smo}^{1/2}}{\sigma_{rms}}, \quad (1)$$

where F_c is in Jy km s^{-1} , W_{50} is in km s^{-1} , w_{smo} is a smoothing width equal to the number of 10 km s^{-1} bins bridging half the signal, and σ_{rms} is the rms noise (in mJy) across the

integrated spectrum at 10 km s^{-1} resolution. The HI mass M_{HI} for each cloud is in col. (7), and is computed assuming that the clouds are optically thin and at the Virgo distance $D_V=16.7 \text{ Mpc}$:

$$M_{HI}/M_{\odot} = 2.356 \times 10^5 D_V^2 F_c , \quad (2)$$

where D_V is in Mpc and F_c is in Jy km s^{-1} . The uncertainties on M_{HI} in Table 2 and elsewhere do not include that in the distance adopted, which is poorly constrained due to the large peculiar velocities of objects near or within the cluster.

2.2. Cloud Morphologies and Kinematics from ALFALFA data

Cloud C1: C1 is the main cloud in the complex and the highest S/N detection in this region. It is marginally resolved by the ALFA beams (Figure 2). Its integrated profile is symmetric and narrow with a peak flux density of 38 mJy (Figure 3). C1 has one of the largest HI masses in the complex at $M_{HI} = (1.62 \pm 0.04) \times 10^8 M_{\odot}$. There is a faint, uncataloged optical feature visible in SDSS images in the vicinity of C1; its relationship to the HI cloud is discussed in Section 5.

Cloud C2: This isolated cloud is the faintest ALFALFA detection in the region at $S/N = 6.5$, and it has the lowest H I mass. C2 is close to the ImV dwarf galaxy VCC 1357 (Binggeli *et al.* 1985), but the ALFALFA centroid is offset from the optical position of the latter by $2'$ to the West. No optical redshift is available for VCC 1357. An Arecibo single-beam observation centered on VCC 1357 with similar sensitivity to the ALFALFA data is presented by Hoffman *et al.* (1987). The properties of their detection are identical to those of C2 within the measurement uncertainties; these and the ALFALFA observations have likely uncovered the same object. However, the previous association of VCC 1357 with this H I source is now in doubt by the evidence for an offset in position between the two, and by the detection of the other H I complex clouds presented here. The positional offset between VCC 1357 and C2 is confirmed by the VLA data discussed in the next section.

The possible relationship between C2 and VCC 1357 is discussed in Section 5.

Cloud C3: This northernmost component of the complex is unresolved by the ALFA beam. Its integrated profile appears asymmetric with more emission on the high velocity side of the peak (Figure 3), but this may be an artifact of the poor S/N . C3 is not connected to the main clouds C1 and C4 at the sensitivity obtained. There is no discernible optical counterpart to C3 in the SDSS or DSS survey images of the region.

Cloud C4: This cloud appears to be connected to the main cloud C1, with its centroid located just $6'.6$ to the North of the latter (Figures 1 and 2). Its H I mass, $M_{HI} = (1.66 \pm 0.08) \times 10^8 M_{\odot}$, is comparable with that of C1 but its integrated profile is significantly broader. The spectrum is asymmetric with more emission on the high-velocity side of the peak (Figure 3), and the cloud is (poorly) resolved into a collection of smaller clumps by the ALFA beam (Figure 1). Line broadening is thus likely to arise from this superposition, rather than from coherent rotation. There is no discernible optical counterpart to C4 in the SDSS or DSS survey images of the region.

Cloud C5: This cloud is located $17'.4$ Southeast of the main cloud C1. Its integrated profile appears to be symmetric, and implies an H I mass that is a third that of C1 at $M_{HI} = (5.9 \pm 0.4) \times 10^7 M_{\odot}$. At the ALFALFA sensitivity, C5 is not connected with any other complex clouds. There is no discernible optical counterpart to C5 in the SDSS or DSS survey images of the region.

3. Aperture Synthesis Follow-up Observations

Aperture synthesis observations of the central region of the cloud complex detected by ALFALFA were obtained with the Very Large Array¹¹ (VLA) in two campaigns. On 2005

¹¹The VLA is a facility of National Radio Astronomy Observatory, which is operated by Associated Universities, Inc., under a cooperative agreement with the National Science

July 11, 5 hours on-source were obtained via rapid response observations in C configuration. On 2006 Jan 18 – 23, dynamically scheduled observations during the D – A configuration change yielded ~ 1.5 hours on-source with antennas that hadn’t yet been moved. All observations had common pointing and spectral centers of $\alpha = 12^{\text{h}} 30^{\text{m}} 45^{\text{s}}$, $\delta = +9^{\circ} 26' 0''$ (J2000) and $\nu = 1417$ MHz, and online Hanning smoothing was applied to yield 48.8 kHz channels over a total bandpass of 3.125 MHz. The observing setup was chosen to maximize the number of ALFALFA cloud detections accessible to the VLA in a single pointing: all of the clouds in Table 2 except C3 fall within the resulting field-of-view and bandpass.

The data from the runs was reduced using the Astronomical Image Processing System (AIPS; Greisen 2003). Standard flux, phase and bandpass calibration routines were applied. Continuum emission was removed from the data via linear fits to the average visibilities in line-free channels spanning 245 kHz at either end of the calibrated bandpass, yielding a net bandwidth of 2.2 MHz sensitive to HI emission.

After calibration, the data from each run were combined into a single UV data cube and imaged using a variety of spatial and spectral weighting schemes. The dirty beam pattern was deconvolved from the data using the Multi-Scale Clean algorithm implemented in AIPS (Cornwell 2008; Greisen *et al.*, in prep.), in which components are extracted from a series of tapered images of the visibilities. We find that the resulting maps are not sensitive to the details of the deconvolution process, and therefore analyze the highest sensitivity, naturally-weighted cube with a synthesized beam width of $22''$ (1.8 kpc at the Virgo distance). All maps and derived parameters are corrected for the attenuation of the primary beam, and averaged over 2 or 3 spectral channels to yield resolutions of $\delta V' = 20.7 \text{ km s}^{-1}$ or $\delta V' = 31.0 \text{ km s}^{-1}$, respectively. A summary of the aperture synthesis observing and map parameters is given in Table 3. For clarity, all variables denoting parameters derived from the VLA observations are primed.

3.1. H I Aperture Synthesis Detections

We make two detections in the VLA data, which correspond to the clouds C1 and C2 identified in the ALFALFA survey data. Channel maps of these detections are shown in Figs. 4 and 5. Contours are at multiples of the median rms map noise σ'_m in the primary beam-corrected maps at that location, and negative contours are indicated by dashed lines. We find that the emission associated with C1 and C2 spans multiple synthesized beams over contiguous (but largely independent¹²) channels irrespective of the visibility weighting or image deconvolution scheme adopted: they are credible detections in the VLA data.

Total intensity and intensity-weighted velocity maps for the clouds are shown in Figs. 6 and 7. The data cubes are blanked before these moments are computed: a mask is generated for each frequency channel by smoothing the data to half the angular resolution in Table 3 and blanking regions with fluxes less than $2\sigma'_m$ of that image. In addition, the intensity-weighted velocity maps in Figs. 6b and 7b are computed only at locations with column density $N'_{HI} \geq 10^{20} \text{ cm}^{-2}$. Integrated spectral profiles for C1 and C2 from the VLA observations are in Figure 8. The 1σ error bars on each point in Fig. 8 reflect σ'_m integrated over the emission region in that channel and a 5% calibration uncertainty.

The properties of C1 and C2 derived from the VLA data are given in Table 4. Unless otherwise indicated, the parameters are computed in the same manner as their ALFALFA counterparts (see Section 2.1). The location of the peak N'_{HI} in the total intensity maps of Figs. 6a and 7a is given in col. (2). The centroid cz'_\odot of the integrated profiles of Figure 8 is in col. (3), and $W50'$ of the profiles is in col. (4). The values of $W50'$ are corrected for instrumental effects by assuming that the unbroadened profile is gaussian. The integrated flux density F'_c and H I mass M'_{HI} are in cols. (5) and (8), respectively. The maximum

¹²The noise in each channel is weakly correlated by the continuum subtraction. We have verified that the details of this subtraction do not impact the detected cloud morphologies.

angular extent a'_{HI} of each cloud is in col. (6). We adopt the outermost locations where $N'_{HI} = 10^{20} \text{ cm}^{-2}$ in Figs. 6a and 7a as the cloud edges, and correct the measured values for beam smearing. The position angle PA'_{HI} at which a'_{HI} is measured is in col. (7). An estimate of the dynamical mass M'_{dyn} of each cloud is in col. (9), and is computed via:

$$M'_{dyn} = (3.39 \times 10^4) a'_{HI} D_V \left(\frac{W50'}{2} \right)^2, \quad (3)$$

where a'_{HI} is the object diameter in arcminutes, $W50'$ is in km s^{-1} and the Virgo distance D_V is in Mpc. We note that M'_{dyn} has physical meaning only if the clouds are self-gravitating and in dynamical equilibrium; these two assumptions may not be valid for C1 and C2 (see Section 6).

Position-velocity slices through the C1 and C2 datacubes are shown in Figs. 9 and 10, respectively. For C1 in Fig.9, one $3''$ -wide slice is oriented along PA'_{HI} , and the other is perpendicular to this axis. We note that the emission is unresolved both spatially and spectrally along the axis perpendicular to PA'_{HI} for C2, and we therefore show only the slice oriented along PA'_{HI} in Fig. 10.

3.2. HI Morphologies and Kinematics of C1 and C2

The VLA follow-up data provide important insight into the H I morphologies and kinematics of C1 and C2.

Cloud C1: Figs. 4 and 6a show that C1 has a disordered morphology at the resolution of the VLA observations, with the bulk of the emission stemming from an arc-like structure at $cz'_{\odot} = 486 \text{ km s}^{-1}$. The apparent “clumpiness” of the detected emission down to the synthesized beam width of $\sim 22''$ (1.8 kpc) is not a deconvolution artifact, and suggests that the cloud exhibits structure on even smaller scales. The box in Fig. 6 a encloses a faint, uncatalogued optical feature that is coincident with a high N'_{HI} peak in C1; we discuss the implications of an association between these optical and HI sources in §6. Figs. 6b and 9

show that the cloud has no coherent velocity structure.

Figs 4 and 6 illustrate that there is very good agreement between the centroid of the C1 emission detected by ALFALFA and that detected by the VLA. The global properties of C1 measured from the VLA data also correspond well with those obtained from the ALFALFA data, although less HI flux is detected in the former ($F'_c/F_c = 86 \pm 4\%$, Tables 2 and 4). If this “missing” flux is uniformly distributed over a circular region at least $1.5'$ across, it would escape detection at the $3\sigma'_m$ level in an optimally smoothed frequency channel of the VLA data. If it is contained in a coherent structure, we expect it to be kinematically coincident with the arc in Fig. 6 since $cz_\odot - cz'_\odot \sim 0$.

Cloud C2: Figs. 5 and 7 illustrate that C2 has a markedly different H I morphology from C1. The emission in each channel of the VLA observations is barely resolved both spatially and spectrally, with the bulk of the emission in an unresolved feature at $\alpha' = 12^h 31^m 18.0^s$, $\delta' = +9^\circ 29' 30''$ (J2000) in the $cz'_\odot = 585 \text{ km s}^{-1}$ channel. The total intensity map of C2 in Fig. 7a consists of two clumps: that to the Northwest results from the brightest H I feature at $cz'_\odot = 585 \text{ km s}^{-1}$, and that to the Southeast results from emission distributed over $585 \text{ km s}^{-1} < cz_\odot < 625 \text{ km s}^{-1}$. Figs. 7b and 9 indicate that there is a $\sim 15 \text{ km s}^{-1}$ gradient in the velocity field of C2. Given the poor sensitivity and resolution of the VLA data across the detection, it remains unclear whether or not this gradient stems from coherent internal motions.

A comparison between the integrated properties of C2 derived from the ALFALFA and VLA observations suggests that a small but statistically significant amount of H I in this source has not been detected by the VLA ($M_{HI} - M'_{HI} = [1.0 \pm 0.5] \times 10^7 M_\odot$; Tables 2 and 4). There are few direct constraints on the morphology of the missing gas. However, given the gradient in the C2 velocity field (Fig. 7b), the quantities $cz_\odot - cz'_\odot = (10 \pm 5) \text{ km s}^{-1}$ and $W50 - W50' = (18 \pm 9) \text{ km s}^{-1}$ are consistent with a kinematically coherent extension to the Southeast beyond that detected at $cz'_\odot = 626 \text{ km s}^{-1}$

in Fig 5.

The star in Figs. 5 and 7a denotes the optical location of VCC 1357 (Binggeli *et al.* 1985). The VLA observations therefore confirm the offset between this source and C2 suggested by the ALFALFA data (§2.2). It is thus clear that if C2 is associated with VCC 1357, then the gas in this system is displaced by $\sim 2'$ (10 kpc in projection, or ~ 10 optical diameters; Binggeli *et al.* 1993) from the stars. We discuss the implications of an association between these H I and optical features in Section 5.

3.3. Non-Detections in the VLA Follow-up Data

While the complex clouds C4 and C5 fall within the field-of-view and bandpass of our VLA observations, they are not detected in the resulting dataset. This is not surprising given their projected distances of $11.2'$ and $12.5'$ from the pointing center in Table 4. Given the integrated spectral profile shapes and centroids of these clouds in the ALFALFA survey data (Table 2), we expect their emission to fall below the $3\sigma'_m$ detection limit in the VLA data cube if they are smoothly distributed over a circular region with a diameter $\gtrsim 1'$. The VLA non-detections therefore provide little insight into the morphologies and kinematics of C4 and C5.

4. CO(3–2) Observations

An exploratory observation of the CO(3–2) emission line consisting of a single pointing (R.A.(J2000) = $12^h30^m27^s$, Dec.(J2000) = $+9^\circ28'34.5''$) was carried out with the APEX Telescope (Güsten *et al.* 2006) located in the Chajnantor Plateau in northern Chile. This pointing was chosen because corresponds to the peak of the HI emission in the VLA map. The observations took place during the night of January 1st, 2008, using the the 345 GHz DSB heterodyne receiver APEX-2A. The beamsize (FWHM) of the APEX 12-m telescope

is $18''$ at 345 GHz. The receiver was tuned to CO(3–2) at $V_{\text{helio}} = 490 \text{ km s}^{-1}$, with a total bandwidth of 1550 km s^{-1} and spectral resolution of 0.8 km s^{-1} . Observations were performed with an atmospheric opacity at 220 GHz of 0.34, with a mean PWV ~ 2.1 mm yielding to a $T_{\text{sys}}(\text{DSB}) = 370 \text{ K}$. Pointing using Saturn as reference was regularly performed and was better than $2''$. The total on-source integration time was 36 min, reaching a rms of 48 mK with a spectral resolution of 0.9 km s^{-1} . The antenna efficiency was estimated at 70%.

Data reduction and analysis were performed using the CLASS package from the GILDAS software (Pety 2005). Reduction consisted of baseline subtraction and the integration of the individual scans. The adjacent channels were re-binned to a velocity resolution of 22.9 km s^{-1} , leading to a rms of 12.9 mK in T_{mb} . No clear detection was found.

These exploratory CO(3–2) observations allow us to place an upper limit to the mass in molecular form in C1. In order to estimate a $3\text{-}\sigma$ upper limit, we assume an expected line width of 50 km s^{-1} , yielding to a $I_{\text{CO}(3-2)} = 1.93 \text{ K km s}^{-1}$. We assume a conversion “X” factor between the CO(1–0) line and the molecular hydrogen column density N_{H_2} of $2.8 \times 10^{20} \text{ cm}^{-2} (\text{km s}^{-1})^{-1}$ (Bloemen *et al.* 1986). We also adopted a CO(3–2)/CO(1–0) integrated line intensity ratio of 0.4 which is the typical value of the Galactic disk (Sanders *et al.* 1993). These values yield a H_2 column density limit for the observation of $N_{\text{H}_2} < 1.3 \times 10^{21} \text{ cm}^{-2}$, averaged over a beam of $18''$. At a distance of 16.7 Mpc, this column density over a $1'$ diameter is equivalent to a molecular hydrogen upper mass limit of $M_{\text{H}_2} < 4.0 \times 10^8 M_{\odot}$, which is comparable to the HI mass (see Table 2.). Allowing for uncertainties in the value of the X factor, the metallicity of the cloud gas, and the CO(3–2)/CO(1–0) integrated line ratio, we can conclude that the gas mass in the cloud C1 is unlikely to be dominated by the molecular component.

5. The Environment of the Cloud Complex

The optical feature of unknown redshift appearing in the field of C1 and discussed in Section 3.2 appears to be just above the SDSS g -band detection limit. If the feature is approximately $\sim 10''$ across, then its g -band luminosity at the Virgo distance would be $L_g \sim 10^6 L_\odot$. The stellar M/L ratios models of Bell *et al.* (2003) give $M^*/L^* \sim 1.6$. If this feature is the optical counterpart of C1, then the stellar to HI mass ratio is less than 0.01 and $M_{HI}/L_g > 170$. An analogous exercise for C2 and the putative counterpart VCC 1357 yields a stellar to HI mass ratio of less than 0.05.

As for the possible optical counterparts of clouds C1 and C2, attempts to obtain optical redshifts were made in two occasions with the Palomar 5m Hale telescope. The first time was unsuccessful due to limited sky transparency, the second due to lack of any discernible H_α emission or of any other measurable spectral signature. The possibility of an association between HI and optical features remains open.

Figure 11 shows the Virgo Cluster X-ray emission in the vicinity of the HI cloud complex (Snowden *et al.* 1995). The large X-ray emission regions are centered on M49 and M87, with the HI cloud complex indicated with the crossed circles. Near the projected location of the cloud complex, Vollmer *et al.* (2001) estimate that the hot intracluster gas (ICM) density is $n_{icm} \sim 10^{-4} \text{ cm}^{-3}$, while Shibata *et al.* (2001) have measured an ICM temperature of $T_8 = 0.235$ in units of 10^8 K .

Several galaxies are projected in the vicinity of the cloud complex. Figure 12 shows all cataloged objects within 1° of C1 and with heliocentric velocities between 100 and 900 km s^{-1} : galaxies detected in the 21cm line are plotted with a circle of area proportional to the HI mass; galaxies not detected in ALFALFA with redshift information from other sources are plotted with crosses, most of which are early type systems. It is assumed that all galaxies are located at the distance of the Virgo cluster. Note that the velocities of the HI clouds range between 480 and 607 km s^{-1} , i.e. if they are part of the Virgo cluster their

line of sight velocity with respect to the cluster reference frame is directed toward us, as the heliocentric velocity of the cluster is 1150 km s^{-1} (Huchra 1988). Under the assumption that the clouds originated in the disk of a galaxy moving at high speed through the cluster, the velocity of the parent galaxy should also be incoming in the cluster reference frame, and most likely doing so at a larger velocity than the clouds themselves, as the latter would be decelerated by ram pressure after stripping. In the heliocentric reference frame, the parent galaxy should then have a *lower* velocity than those in the cloud complex. Two objects satisfy that condition: NGC 4424 and NGC 4445. Their locations are indicated by a plus sign (NGC 4424) and X symbol (NGC 4445) in Figure 11. In addition, as we discuss below, they are also extremely gas deficient for their size, which is evidence that they have been stripped within the last passage through the cluster.

The SBa galaxy NGC 4424 (also known as UGC 7561 and VCC 9079) is located at $\alpha = 12^{\text{h}}27^{\text{m}}11.6^{\text{s}}, \delta = +09^{\circ}25'14''$ (J2000). This places NGC 4424 at a projected distance of 236 kpc from the cloud center, and 900 kpc from M87. This peculiar galaxy is at a velocity ($cz_{\odot}=437 \text{ km s}^{-1}$), near that of the main cloud. The angular size of the stellar component, $3'.6 \times 1'.8$, translates to a linear size of $17 \times 9 \text{ kpc}$ at the Virgo distance. A detailed study by Cortes *et al.* (2006) characterizes it as having disturbed morphology; they also suggest that CO observations are indicative of non-circular gas motions and discuss convincingly the vulnerability of the galaxy to ram pressure stripping (see also Kenney *et al.* 1996). NGC 4424 has a HI mass of $2.5 \times 10^8 M_{\odot}$ and estimations of HI deficiency values have been reported between of 0.75 (Chung *et al.* 2007) and 1.09 (Helou *et al.* 1984). Those figures indicate that NGC 4424 has lost between 80% and 90% of its HI gas. Chung *et al.* (2007) noted that NGC 4424 exhibits a one-sided tail extending to the southeast, which is also detected by ALFALFA, and that the HI disk is truncated at a radius smaller than that of the stellar component of the galaxy. The direction of the tail shows the southeast to northwest direction of motion for NGC 4424; this motion is not compatible with the position of the cloud complex.

NGC 4445 (also known as UGC 7587 and VCC 1086) is an edge on spiral, possibly of type Sab, located at $\alpha = 12^{\text{h}}28^{\text{m}}15.9^{\text{s}}, \delta = +09^{\circ}26'11''$ (J2000). Its heliocentric radial velocity is $cz_{\odot}=354 \text{ km s}^{-1}$ and the HI mass $5.5 \times 10^7 M_{\odot}$ (Kent *et al.* 2008). Solanes *et al.* (2002) estimate its HI deficiency between 0.98 and 1.11, i.e. NGC 4445 has lost about between 90% and 93% of its HI gas. With a major axis angular diameter of $2'.6$, its linear size is about 13 kpc. We are not aware of HI synthesis data of this object; none are found in the VLA data archive.

6. Discussion

One possibility that deems consideration is that the clouds are gravitationally bound structures, embedded in their own dark matter halos. If an HI cloud is gravitationally bound, its total dynamical mass within the HI radius can be computed from Equation 3, assuming spherical symmetry. Such mass is $2.3 \times 10^9 M_{\odot}$ for C1 and $0.3 \times 10^9 M_{\odot}$ for C2 as calculated from the aperture synthesis measurements. The density of such objects would be $1.4 \times 10^{-25} \text{ g cm}^{-3}$ for C1 and $1.0 \times 10^{-25} \text{ g cm}^{-3}$ for C2. These densities can be compared to the critical density, $\rho_{crit} = (1.9 \times 10^{-29} \text{ g cm}^{-3}) h^2$, where $h = 0.7$. Were dark matter to provide the gravitational binding and to extend well beyond the visible, baryonic component, the total halo mass of, e.g., C1 would exceed $10^{10} M_{\odot}$. In that case, it would be surprising that the VLA data do not exhibit any trace of ordered motions in the gas, nor does the visible matter show any degree of central concentration, thus violating the mass–concentration relation for halos. A similar issue can be raised for the whole cloud complex. If bound by self–gravity, its total dynamical mass would be of order of $10^{11} M_{\odot}$ and its mean density $2.1 \times 10^{-27} \text{ g cm}^{-3}$. Again, the cloud complex shows no ordered motions. The possibility that the clouds in the complex are a group of optically dark galaxies embedded in their own dark matter halo appears relatively implausible.

For a purely gravitational event, we may expect stream-like topology in the removed

gas, which is not observed. High speed galaxy-galaxy encounters tend to produce relatively small damage in terms of gas mass loss by the victim, albeit spectacular in spatial extent as in the case of NGC 4254/VirgoHI21. For NGC 4424 and NGC 4445, the damage would have been quite substantial (more HI is seen in the cloud complex than in either of the galaxies themselves) and the topology of the remnant is not particularly stream-like. These are not however very strong arguments and the possible origin through a high speed close encounter cannot be excluded.

Ram pressure stripping is very likely if the galaxy’s orbit takes it deep in the cluster potential well, and can result in severe gas depletion from its outer disk (Cortés *et al.* 2006). With a radial velocity differing from the systemic velocity of the cluster by 700 km s^{-1} and a projected location half way between M87 and M49, the likelihood that ram pressure is currently very effective is marginal; it could however have been far more effective a few 10^8 years ago, if the orbit dipped closer to the cluster center, independently on whether or not an encounter or merger took place. As we will see, that likelihood is even higher for NGC 4445.

6.1. Orbital Motion Through the ICM: a Simple Simulation

We consider the motion of a galaxy as it dips into the ICM on a parabolic orbit of pericluster distance r_p . Parametrized by the azimuthal angle ϕ , as illustrated in Figure 13, the distance of the galaxy from the focal point (M87) is

$$r = \frac{2r_p}{1 + \cos \phi} \quad (4)$$

while the orbital escape velocity is

$$v_g = \sqrt{\frac{2GM_{clu}}{r}} \quad (5)$$

where M_{clu} is the cluster mass. For simplicity, we assume the cluster mass is concentrated in M87 and equal to $10^{14} M_\odot$, rather than integrating the motion for a changing cluster

mass within the variable r , which is sufficient for our purposes. For the ICM density n_{icm} we assume the β -model (Schindler, Binggeli & Boehringer 1999; Vollmer *et al.* 2001), given by

$$n_{icm} = n_0(1 + r^2/r_{clu}^2)^{-3\beta/2} \quad (6)$$

with a central density of $n_0 = 0.04 \text{ cm}^{-3}$ and a core radius of $r_{clu} = 21 \text{ kpc}$, appropriate for the SW sector of the cluster and $r_{clu} = 13.4 \text{ kpc}$ for the cluster as a whole.

As the galaxy travels through the ICM, we assume the galactic gas is stripped at pericenter; from there on, we estimate the ram acceleration and integrate the growing separation Δr and Δv between the galaxy and clouds. Figure 14 shows the orbital parameters for pericenter distances of $r_p = 400, 500$, and 600 kpc . The best orbit in this simple exercise is fit with $r_p \sim 500 \text{ kpc}$. In that scenario, a galaxy reaches a distance $r = 1100 \text{ kpc}$, 1.0 Gyr after pericenter passage. The velocity of the galaxy at $r = 1100 \text{ kpc}$ is 1100 km s^{-1} . Velocity (Δv) and spatial (Δr) separation values of 200 kpc and 300 km s^{-1} respectively are obtained from Figure 14. Corrections for the inclination along the line-of-sight for $\theta \sim 45^\circ$ give values of $\Delta r \sim 140 \text{ kpc}$ and $\Delta v \sim 200 \text{ km s}^{-1}$. These numbers are in general agreement with the observed values.

6.2. Possible Formation Mechanisms

We can now consider two possible scenarios of cloud formation as the galaxy moves through the cluster: (a) removal by ram pressure and (b) a high speed tidal interaction, of the type responsible for VirgoHI21 (Duc & Bournaud 2008; Haynes *et al.* 2007).

Ram pressure stripping will occur when the ram pressure arising from the motion of the galaxy at velocity $v_{gal,3d}$ with respect to the intracluster medium of number density n_{icm} , $n_{icm}m_p v_{gal,3d}^2$ (where m_p is the proton mass), exceeds the restoring gravitational force that binds the gas to the galaxy: $2\pi G \Sigma_{ism} \Sigma_d$, where Σ_{ism} is the gas surface density of the galactic disk and Σ_d is the total surface mass density of the disk. This condition can be

rewritten as

$$\left(\frac{n_{icm}}{10^{-3} \text{ cm}^{-3}}\right) \left(\frac{v_{gal,3d}}{10^3 \text{ km s}^{-1}}\right)^2 \geq 11 \left(\frac{M_d}{10^{11} M_\odot}\right)^2 \left(\frac{R_{gal}}{10 \text{ kpc}}\right)^{-4} \left(\frac{M_{ism}}{0.1 M_d}\right) \quad (7)$$

where M_d and M_{ism} are now the total disk and gas masses within the radius R_{gal} .

At the location of the cloud complex, some 845 kpc from M87, the density of the intracluster gas (ICM) is significantly lower than near the center of the cluster. For a β -model (Eqn. 6) at the present projected distance of the clouds from M87, $n_{icm} \sim 10^{-4} \text{ cm}^{-3}$. In the case of NGC 4424, $v_{gal,3d} \simeq 700 / \cos \theta \text{ km s}^{-1}$, where θ is the angle between the line of sight and the galaxy velocity vector. We estimate a disk mass enclosed within $R_{gal} \simeq 10 \text{ kpc}$ of about $10^{10} M_\odot$ (a generous estimate, since the total velocity width of the HI emission of the galaxy is 61 km s^{-1} (Kent *et al.* 2008) and the inclination of the disk, albeit unknown, is unlikely to be smaller than 45°) and assume $M_{ism}/0.1M_d \sim 1$. With those numbers, the ram pressure term roughly matches the restoring force at the larger galactocentric radii. Chung *et al.* (2007) also compute ram pressure effects in the range between $125 < n_{icm} v_{gal}^2 < 175 \text{ cm}^{-3} (\text{km s}^{-1})^2$ and a restoring force range between $40 < \Sigma_{ism} V_{rot}^2 / R_{gal} < 475 \text{ cm}^{-3} (\text{km s}^{-1})^2$ for NGC 4424.

In the case of NGC 4445, $v_{gal,3d} \simeq 800 / \cos \theta \text{ km s}^{-1}$. The radial extent of the HI disk is currently unknown, but we can estimate the ram pressure and the restoring force at $R_{gal} \simeq 6 \text{ kpc}$, as well as its disk mass from a rotational velocity of 107 km s^{-1} , from the measured velocity full width of the HI line of 213 km s^{-1} . Again, the ram pressure term is comparable with the restoring force at the galactocentric radii at which most of the HI would be expected to be found in an unperturbed disk.

It is interesting to point out that NGC 4522, a very clear case of ram pressure stripping carefully studied by Kenney *et al.* (2004), is projected on the same region of the cluster (RA=12^h 33^m 39.7^s, Dec=09° 10'30'') albeit in a different velocity regime ($cz = 2307 \text{ km s}^{-1}$). At the present location, Kenney *et al.* argue that the ICM density as described by the smooth β -model of eqn. 6 is likely to be inadequate to explain the stripping. They

invoke the possibility that the ICM may be locally denser than implied by the model.

6.3. Timing Considerations

Estimates of the tidal effects can be made by considering two nearby clouds in the vicinity of a cluster (Figure 15). The two clouds will disperse at a rate $\Delta v = g\Delta t$ under the gravitational tidal acceleration g from the cluster potential, where g is

$$g = \frac{2GM_{cluster}x}{R_{cluster}^3} \quad (8)$$

where $M_{cluster}$ is the mass of the cluster within radius $R_{cluster}$, and x is the initial separation of the two clouds. The timescale of the encounter can be taken as $\Delta t \sim R_{cluster}/v_{c,3d}$, where $v_{c,3d} = v_c/\cos\theta$ is the velocity of the cloud complex with respect to the cluster. Taking $\Delta v = g\Delta t$, we can write a simple relation for the separation rate of the two clouds

$$\Delta v \approx \frac{2GM_{cluster}x}{R_{cluster}^2 v_{c,3d}} \quad (9)$$

Two clouds initially separated by 10 kpc, located 845 kpc from the center of the cluster of mass $10^{14} M_\odot$ and moving at a velocity of $600/\cos\theta \text{ km s}^{-1}$ with respect to the cluster would roughly double their separation in a time comparable with the cluster crossing time. Tidal forces related to the cluster potential alone are unlikely to account for the spatial dispersion of the clouds in the complex, if they were stripped from a single galaxy.

The cloud complex is separated by $\Delta r \sim 235/\sin\theta$ kpc and by $\Delta v \sim 100/\cos\theta \text{ km s}^{-1}$ in velocity from NGC 4424; the corresponding numbers for NGC 4445 are respectively $\Delta r \sim 150/\sin\theta$ kpc $\Delta v \sim 200/\cos\theta \text{ km s}^{-1}$. This separation would increase from zero to the observed value over a time of order

$$\Delta t_{sep,4424} \sim 2.3(\tan\theta)^{-1} \text{ Gyr} \quad (10)$$

for NGC 4424 and

$$\Delta t_{sep,4445} \sim 0.7(\tan\theta)^{-1} \text{ Gyr}. \quad (11)$$

for NGC 4445. For relatively large values of θ , they can be comparable with the time it takes for the galaxy to cross the inner regions of the cluster $R_{cluster}/v_{gal,3d}$. Under constant acceleration, the time necessary to reach the observed values of Δv and Δr would be about twice Δt_{sep} as computed above. Either of those assumptions are unrealistic if ram pressure acts upon the clouds, as they travel through an ICM of variable density. However, two preliminary conclusions can be made already: (i) if the clouds originated from NGC 4445 or NGC 4424, the stripping took place at least a few 10^8 yrs ago; (ii) simple kinematic timescales make NGC 4445 as a more palatable candidate as a parent galaxy than NGC 4424. In the following, we concentrate our discussion on the assumption that the clouds were stripped from NGC 4445, although we maintain the inferred relations parametrized form for easy application to NGC 4424. Next, we derive the acceleration due to ram pressure.

As a spherical cloud of radius r_c travels through the ICM at speed $v_{c,3d} = v_c / \cos \theta$, the force acting on its surface can be written as the ram pressure times the area, given by

$$F = n_{icm} m_p v_{c,3d}^2 \pi r_c^2. \quad (12)$$

The resulting acceleration due to ram pressure is

$$a_{rp} = \Delta v / \Delta t = \frac{\rho_{icm} v_{c,3d}^2 \pi r_c^2 \eta}{M_{HI}} \quad (13)$$

where the factor η accounts for the fraction of gas in form other than HI and M_{HI} is the HI mass of the cloud. The acceleration can then be written as

$$a_{rp} = 2.5 \times 10^{-9} \eta \left(\frac{n_{icm}}{10^{-3} \text{ cm}^{-3}} \right) \left(\frac{r_c}{\text{kpc}} \right)^2 \left(\frac{v_{c,3d}}{10^3 \text{ km s}^{-1}} \right)^2 \left(\frac{M_{HI}}{10^8 M_\odot} \right)^{-1} [\text{cm s}^{-2}] \quad (14)$$

Once the gas is stripped, while the motion of the galaxy is relatively unimpeded by the ram pressure, the clouds fall behind, affected by the acceleration a . In order to accumulate a velocity difference from the galaxy Δv , at constant acceleration a time on order of $\Delta t_v = \Delta v / a$ will be required, while in order to accumulate a separation Δr , a time on order

of $\Delta t_r = (2\Delta r/a)^{1/2}$ will be required:

$$\Delta t_v = 1.3 \times 10^8 \text{ yr} \left(\frac{\Delta v}{10^2 \text{ km s}^{-1}} \right) A \cos \theta \quad (15)$$

$$\Delta t_r = 5.0 \times 10^8 \text{ yr} \left(\frac{\Delta r}{10^2 \text{ kpc}} \right)^{1/2} A^{1/2} \cos \theta \sin^{-1/2} \theta \quad (16)$$

where

$$A = \eta^{-1} \left(\frac{n_{icm}}{10^{-3} \text{ cm}^{-3}} \right)^{-1} \left(\frac{v_c}{10^3 \text{ km s}^{-1}} \right)^{-2} \left(\frac{r_c}{\text{kpc}} \right)^{-2} \left(\frac{M_{HI}}{10^8 M_\odot} \right) \quad (17)$$

For cloud C1, $M_{HI} = 1.6 \times 10^8 M_\odot$. The maximum radius out to which the VLA detects HI emission in C1 is about $1'.3$, which translates to 6.5 kpc at the Virgo cluster distance. However, the *effective* radius of the cloud is very likely smaller than 6.5 kpc. A cursory inspection of Figure 6 shows that only about $1/3$ of the area subtended by the emission out to a $1'$ radius exceeds a column density of gas at half the peak level, which would yield an effective radius of order of 3 kpc. In addition, from the topology of the HI gas in our own ISM, it is found that while the majority of the HI emission arises in denser regions, those clouds' volume filling factor is quite small. Such structure would be unresolved by the $22''$ (1.8 kpc) beam of the VLA observations. Values of order $r_c = 2\text{--}4$ kpc appear appropriate. The parameter η , which accounts for the mass fraction of He and other than HI gas, should be in the range 0.4–0.7. Near the current location of the clouds, the ICM density is unlikely to exceed $n_{icm} \simeq 10^{-4} \text{ cm}^{-3}$, unless the ICM is very clumpy, as suggested by Kenney *et al.* (2004). As for the parameters specific for the galaxies, for NGC 4424 $v_c = 700 \text{ km s}^{-1}$, $\Delta r = 235 \text{ kpc}$ and $\Delta v = 100 \text{ km s}^{-1}$, while for NGC 4445 $v_c = 800 \text{ km s}^{-1}$, $\Delta r = 150 \text{ kpc}$ and $\Delta v = 200 \text{ km s}^{-1}$. Note that by imposing $\Delta t_v \simeq \Delta t_r \simeq 2\Delta t_{sep}$ we can obtain a constraint on the combination of physical parameters

$$0.26 A^{1/2} \left(\frac{\Delta v}{10^2 \text{ km s}^{-1}} \right) \left(\frac{\Delta r}{10^2 \text{ kpc}} \right)^{1/2} \sin^{1/2} \theta = 1 \quad (18)$$

As we discussed earlier, accumulation of distance and velocity offsets between clouds and parent galaxy, Δr and Δv , at either constant rate or constant acceleration are used under outlined above, and do not take into account projection effects, which would account for

the orientation of NGC 4445 and the clouds with respect to M87 at the cluster center. It is important to note that a connection between NGC 4445 and the cloud complex is somewhat ambiguous, especially when compared to other disrupted gas features like NGC 4388 which show a clear connection in the form of a tail.

6.4. Evaporation Timescale

According to our findings, if the clouds were stripped from a parent galaxy, most of the stripping took place a fair fraction of a Gyr ago. In that case, it is reasonable to investigate the survival of the clouds in the ICM. Differential ram pressure forces will lead to ablation and dilution of the gas clouds. In addition, upon removal from the galaxy, the cold gas can be heated by conduction by the intracluster gas and the gas mass of the cloud would thus be progressively reduced by evaporation, if (presumably absent) stellar mass loss does not replenish the gas. The evaporation rate in $M_\odot \text{ yr}^{-1}$ can be written as (Cowie & Songaila 1977)

$$\dot{M}_{ev} \simeq 16\pi\mu m_p \kappa r_{kpc}/25k \simeq 35 T_8^{5/2} r_{kpc} (40/\ln \Lambda) M_\odot \text{ yr}^{-1} \quad (19)$$

where μ is the mean molecular weight, m_p the proton mass, κ the thermal conductivity, T_8 the intracluster gas temperature in units of 10^8 K, r_{kpc} the effective cloud radius in kpc (proportional to the square root of the area of the cloud exposed to the ICM), k the Boltzmann constant and $\ln \Lambda$ the Coulomb logarithm. For $T_8 = 0.235$ (Shibata *et al.* 2001) and $40/\ln \Lambda \sim 1$, the evaporation timescale is

$$t_{ev} = M_{gas}/\dot{M}_{ev} \geq 1.7 \times 10^8 r_{kpc}^{-1} \eta^{-1} \psi^{-1} \text{ yr}, \quad (20)$$

where $\psi \leq 1$ is a correction factor roughly proportional to the fraction of the time the cloud's orbit – between the time the gas is removed from the disk and the time of observations — places it in a part of the ICM within which the conductivity coefficient yields the evaporation rate in Eqn. 19. This estimate is very uncertain due to the largely unknown geometry of the cloud, an exact knowledge of its orbit through the ICM, the

unknown fraction of the gas in ionized form and the possible presence of magnetic fields, which would inhibit conduction across field lines. It is clear from Eqn. 20 that if the HI gas is stripped from the galaxy in a region deep enough in the cluster ICM, conduction can obliterate evidence of the cold gas on timescales of $< 10^8$ yr. However, the rate in Eqn. 20 is approximately valid only in vicinity of the cluster core. Away from the central and denser parts of the cluster conduction becomes decreasingly effective, due to the rapid increase of the mean free path of electrons and conduction becoming saturated: this is thought to take place a couple of cluster ICM core radii (~ 50 kpc) out from the center of the ICM distribution (Sarazin 1986). This is why in the simulation described in the preceding section, we have maintained the closest approach of the galaxy to M87, r_p , at values greater than a few hundred kpc; the evaporation timescale remains higher than the kinematical ones and the clouds can be preserved.

7. Summary

We have utilized datasets from the ALFALFA survey and follow-up observations with the Very Large Array to obtain both single dish and aperture synthesis observations of a new HI cloud complex in the Virgo Cluster. The results of these observations are summarized as follows:

1. Five separate HI clouds in the ALFALFA survey have been discovered with radial velocities between $cz_{\odot} \sim 500$ and 600 km s^{-1} . The complex subtends an angle of $35'$ (170 kpc), the individual cloud HI masses range from 0.48 to $1.7 \times 10^8 M_{\odot}$ and the overall HI mass of the complex is $5.1 \times 10^8 M_{\odot}$, at the distance of the Virgo cluster. The clouds' velocity widths vary between 50 and 250 km s^{-1} . In the latter case, the wide spectrum is likely to be due to a blend of several poorly resolved clumps.
2. Several cluster galaxies are found in the vicinity of the cloud complex; the most

likely candidates for association with the clouds are NGC 4424, a disturbed SBa with $cz_{\odot} = 437 \text{ km s}^{-1}$ at a projected distance of 235 kpc from the center of the cloud complex, and NGC 4445, an edge on spiral at a projected distance of 150 kpc, with $cz_{\odot} = 354 \text{ km s}^{-1}$. Both galaxies are extremely HI deficient, apparently having lost between 80% and 93% of their HI gas. The total HI mass of the cloud complex is equivalent to between 1/2 and 1/3 of the HI lost by NGC 4424 and about 4/5 of the HI lost by NGC 4445.

3. Two of the clouds in the complex (C1 and C2) have been detected with the VLA. They have angular sizes of $2.7'$ and $1.5'$ respectively. The synthesis maps do not exhibit any degree of symmetry in the gas distribution or in the velocity field. Faint optical features are found in the vicinity of the two clouds. Lack of optical redshifts prevent us from establishing a physical association. If the optical features were associated with the two clouds, their HI mass to g -band luminosity ratios would be respectively $M_{HI}/L_g \sim 170$ for C1 and $M_{HI}/L_g \sim 30$ for C2, in solar units. A handle on the HI size allows estimates of the dynamical masses of the clouds, contained within the HI radius and under the hypothesis that they are self-gravitating. Those values are $2.3 \times 10^9 M_{\odot}$ for C1 and $0.3 \times 10^9 M_{\odot}$ for C2.
4. The possibility that the clouds constitute a group of primordial structures, embedded in their own dark matter halos, appears unlikely. A more plausible scenario is that the complex is material removed from a galaxy traveling through the cluster at high speed, such as NGC 4424 or NGC 4445. A ram pressure stripping event is preferred to a purely gravitational one.
5. A simulation of plausible orbital parameters for the putative parent galaxy was carried out showing that a nearly radial orbit that would take it to within 400 kpc from M87 would produce effects comparable with those observed. Nearest approach to M87 would have resulted $\sim 1 \text{ Gyr}$ ago, at which stripping of most of the gas is assumed to

have taken place. The nearest approach to the cluster center would be approximately 500 kpc. At that distance from M87, thermal conduction would be ineffective at evaporating the clouds after removal from the parent galaxy. At pericenter passage, the velocity (not corrected for l.o.s. inclination) of the galaxy would be 1100 km s^{-1} . The inclination of the orbital plane to the line of sight of the best fit simulation would be approximately 45° .

6. Dynamical timescales, based on relative velocities and spatial displacements of the clouds from the putative parent galaxy, suggest that the most likely such parent is NGC 4445.

This research has made use of the NASA/IPAC Extragalactic Database (NED) which is operated by the Jet Propulsion Laboratory, California Institute of Technology, under contract with the National Aeronautics and Space Administration. *Skyview* was developed and maintained under NASA ADP Grant NAS5-32068 under the auspices of the High Energy Astrophysics Science Archive Research Center at the Goddard Space Flight Center Laboratory of NASA. KS acknowledges support from a Jansky Fellowship during the completion of this work. This work has been supported by NSF grants AST-0307661, AST-0435697, AST-0607007 and the Brinson Foundation.

This research has made use of Sloan Digital Sky Survey (SDSS) data. Funding for the SDSS has been provided by the Alfred P. Sloan Foundation, the Participating Institutions, the National Aeronautics and Space Administration, the National Science Foundation, the U.S. Department of Energy, the Japanese Monbukagakusho, and the Max Planck Society. The SDSS Web site is <http://www.sdss.org/>. The SDSS is managed by the Astrophysical Research Consortium (ARC) for the Participating Institutions. The Participating Institutions are The University of Chicago, Fermilab, the Institute for Advanced Study, the Japan Participation Group, The Johns Hopkins University, the Korean Scientist Group, Los Alamos National Laboratory, the Max-Planck-Institute for Astronomy

(MPIA), the Max-Planck-Institute for Astrophysics (MPA), New Mexico State University, University of Pittsburgh, University of Portsmouth, Princeton University, the United States Naval Observatory, and the University of Washington.

REFERENCES

- Barnes, D. G. et al. 2001, MNRAS, 322, 486
- Bell, E. F., McIntosh, D. H., Katz, N., & Weinberg, M. D. 2003, ApJS, 149, 289
- Binggeli, B., Sandage, A., & Tammann, G. A. 1985, AJ, 90, 1681
- Binggeli, B., Popescu, C. C., & Tammann, G. A. 1993, A&AS, 98, 275
- Bloemen, J. B. G. L., et al. 1986, A&A, 154, 25
- Cayatte, V., van Gorkom, J.H., Balkowski, C., & Kotanyi, C. 1990, AJ, 100, 604
- Cayatte, V., van Gorkom, J.H., Balkowski, C., & Kotanyi, C. 1994, AJ, 107, 1003
- Chamaraux, P., Balkowski, C., & Gerard, E. 1980, A&A, 83, 38
- Chung, A., van Gorkom, J. H., Kenney, J. D. P., & Vollmer, B. 2007, ApJL, 659, L115
- Chengalur, J. N., Giovanelli, R., & Haynes, M. P. 1995, AJ, 109, 2415
- Cornwell, T. J. 2008, ArXiv e-prints, 806, arXiv:0806.2228
- Cortes, J. R., Kenney, J. D. P., Hardy, E. 2006, AJ, 131, 747
- Cowie, L. L., & Songaila, A. 1977, Nature, 266, 501
- Davies, R. D., & Lewis, B. M. 1973, MNRAS, 165, 231
- Djorgovski, S. 1990, AJ, 99, 31
- Duc, P.-A., & Bournaud, F. 2008, ApJ, 673, 787
- Gavazzi, G., Boselli, A., Donati, A., Franzetti, P. and Scodeggio, M. 2003, *a*, 400, 451
- Giovanelli, R. *et al.* 2005a, AJ, 130, 2598
- Giovanelli, R. & Haynes, M. P. 1989, ApJL, 346, L5

- Giovanelli, R., & Haynes, M. P. 1985, ApJ, 292, 404
- Giovanelli, R., & Haynes, M. P. 1983, AJ, 88, 881
- Giovanelli, R. *et al.* 2007, AJ, 133, 2569
- Greisen, E. W. 2003, Astrophysics and Space Science Library, 285, 109
- Güsten, R. *et al.* 2006, Society of Photo-Optical Instrumentation Engineers (SPIE) Conference, Vol 6267, Ground-based and Airborne Telescopes. Edited by Steep, Larry M. Proceedings of SPIE, Volume 6267, pp. 626714.
- Haynes, M. P., Giovanelli, R., & Chincarini, G. L. 1984, ARA&A, 22, 445
- Haynes, M. P., & Giovanelli, R. 1986, ApJ, 306, 466
- Haynes, M. P., Giovanelli, R., & Kent, B. R. 2007, ApJL, 665, L19
- Helou, G., Hoffman, G. L., & Salpeter, E. E. 1984, ApJS, 55, 433
- Hibbard, J. E., van der Hulst, J. M., Barnes, J. E., & Rich, R. M. 2001, AJ, 122, 2969
- Hoffman, G. L., Helou, G., Salpeter, E. E., & Lewis, B. M. 1989, ApJ, 339, 812
- Hoffman, G. L., Helou, G., Salpeter, E. E., Glosson, J., & Sandage, A. 1987, ApJS, 63, 247
- Huchra, J. P. 1988, in ASP Conf. Ser. 4, The Extragalactic Distance Scale, ed. S. van den Bergh & C.J. Prichet (Salt Lake City: ASP), 257
- Kenney, J. D. P., Koopmann, R. A., Rubin, V. C., & Young, J. S. 1996, AJ, 111, 152
- Kenney, J. D. P., van Gorkom, J. H., & Vollmer, B. 2004, AJ, 127, 3361
- Kent, B. R. *et al.* 2007, AJ, 665, L15
- Kent, B. R., Giovanelli, R., Haynes, M. P. *et al.* 2008, AJ, 136, 713

- Kent, B. R. 2008, Ph.D. Thesis, Cornell University
- Kilborn, V. A., et al. 2000, AJ, 120, 1342
- Koopmann, R.A. *et al.* , 2008, ApJL, accepted
- Lasker, B. M., Sturch, C. R., McLean, B. J., Russell, J. L., Jenkner, H., & Shara, M. M. 1990, AJ, 99, 2019
- Mei, S. *et al.* 2007, ApJ, 655, 144
- Mihos, J. C., Harding, P., Feldmeier, J., & Morrison, H. 2005, ApJL, 631, L41
- Minchin, R. *et al.* . 2005, ApJL, 622, L21
- Minchin, R., et al. 2007, ApJ, 670, 1056
- Moore, B., Katz, N., Lake, G., Dressler, A., & Oemler, A., Jr. 1996, Nature, 379, 613
- Oosterloo, T. & van Gorkom, K. 2005, A&A, 437, L19
- Pety, J. 2005, in SF2A-2005: Semaine de l’Astrophysique Francaise, ed. F. Casoli, T. Contini, J. M. Hameury, & L. Pagani, 721
- Ryder, S. D., et al. 2001, ApJ, 555, 232
- Saintonge, A. 2007, AJ, 133, 2087
- Salzer, J. J., Alighieri, S. D., Matteucci, F., Giovanelli, R. & Haynes, M. P. 1991, AJ, 101, 1258
- Sancisi, R., Thonnard, N., & Ekers, R. D. 1987, ApJL, 315, L39
- Sanders, D. B., Scoville, N. Z., Tilanus, R. P. J., Wang, Z., & Zou, S. 1993, AIP Conf. Proc., 278, 311
- Sarazin, C. L. 1986, Reviews of Modern Physics, 58, 1

- Schindler, S., Binggeli, B., Böhringer, H. 1999, A&A, 343, 420
- Schneider, S. E., Helou, G., Salpeter, E. E., & Terzian, Y. 1983, ApJL, 273, L1
- Shibata *et al.* 2001 ApJ, 49, 228
- Snowden, S. L. *et al.* 1995, ApJ, 454, 643
- Solanes, J. M., Sanchis, T., Salvador-Solé, E., Giovanelli, R., & Haynes, M. P. 2002, AJ, 124, 2440
- Verde, L., Oh, S. P., & Jimenez, R. 2002, MNRAS, 336, 541
- Vollmer, B., Cayatte, V., Balkowski, C., & Duschl, W. J. 2001, ApJ, 561, 708
- York, D. G., et al. 2000, AJ, 120, 1579

Table 1. ALFALFA Observing and Data Cube Parameters

Parameter	Value
Sky center (J2000)	12 20 00, +09 00 00
Spectral range	25 MHz (-2000 – 3200 km s ⁻¹)
Effective integration time	48 seconds (beam solid angle) ⁻¹
Spectral resolution δV	24.4 kHz (5.1 km s ⁻¹)
Half-power beam size	3'.3 × 3'.8
RMS noise σ_m for $\delta V = 5.1$ km s ⁻¹	2.5 mJy/beam

Table 2. Single-Dish Cloud Properties from ALFALFA Survey

Cloud	α, δ (J2000)	cz_{\odot} (km s ⁻¹)	$W50$ (km s ⁻¹)	F_c (Jy km s ⁻¹)	S/N	$\log(M_{HI}/M_{\odot})$
(1)	(2)	(3)	(4)	(5)	(6)	(7)
C1	12 30 25.8, +09 28 01	488 ± 5	62 ± 11	2.48 ± 0.07	21.2	8.21
C2	12 31 19.0, +09 27 49	607 ± 4	56 ± 7	0.72 ± 0.06	6.5	7.67
C3	12 29 42.8, +09 41 54	524 ± 7	116 ± 15	1.16 ± 0.07	8.6	7.87
C4	12 30 19.4, +09 35 18	603 ± 4	252 ± 7	2.56 ± 0.09	13.1	8.22
C5	12 31 26.7, +09 18 52	480 ± 10	53 ± 21	0.91 ± 0.06	7.6	7.77

Note. — Col. (1): cloud name. Col. (2): right ascension and declination of cloud centroid (J2000). Col. (3): average heliocentric velocity of integrated spectral profile from Figure 3. Col. (4): profile width, measured at 50% of the integrated spectra profile peak and corrected for instrumental broadening as described in Giovanelli *et al.* (2007). Col. (5): total flux of integrated spectral profile. Col. (6): signal-to-noise ratio of the detection, computed using $W50$ and F_c via eq. 1. Col. (7): base 10 logarithm of total HI mass, computed using F_c via eq. 2.

Table 3. Aperture Synthesis Observing and Data Cube Parameters

Parameter	Value
Pointing center (J2000)	12 30 45, +09 26 00
Total time on-source	265 min
Net bandpass	2.2 MHz (378 – 822 km s ⁻¹)
Maximum spectral resolution $\delta V'$	48.8 kHz (10.3 km s ⁻¹)
Natural Weighting:	
Synthesized beam	22.2'' \times 20.7'' @ -20°
σ'_m at pointing center, $\delta V' = 20.7$ km s ⁻¹	0.33 mJy/beam
σ'_m at pointing center, $\delta V' = 31.0$ km s ⁻¹	0.29 mJy/beam

Table 4. Aperture Synthesis Cloud Properties from the VLA Observations

Feature	$(\alpha, \delta)'$ (J2000)	cz'_{\odot} (km s $^{-1}$)	$W50'$ (km s $^{-1}$)	F'_c (Jy km s $^{-1}$)	a'_{HI} (')	PA'_{HI} ($^{\circ}$)	$\log(M'_{HI}/M_{\odot})$	$\log(M'_{dyn}/M_{\odot})$
(1)	(2)	(3)	(4)	(5)	(6)	(7)	(8)	(9)
C1	12 30 24 +09 28 20	488 ± 6	78 ± 11	2.14 ± 0.07	2.7 ± 0.3	36	8.15	9.36
C2	12 31 18 +09 29 25	597 ± 3	38 ± 5	0.57 ± 0.06	1.5 ± 0.3	146	7.57	8.48

Note. — Col. (1): cloud name. Col. (2): right ascension and declination of the peak N'_{HI} (J2000). Col. (3): average heliocentric velocity of integrated spectral profile from Figure 8. Col. (4): profile width, measured at 50% of the integrated spectral profile peak and corrected for instrumental effects assuming that unbroadened profile is gaussian. Col. (5): total flux of integrated spectral profile. Col. (6): maximum linear extent of region with $N'_{HI} \geq 10^{20}$ cm $^{-2}$ in the total intensity maps (Figs 6a and 7a). Col. (7): position angle at which a'_{HI} was measured. Col. (8): base 10 logarithm of total H I mass, computed using F'_c via eq. 2. Col. (9): base 10 logarithm of the dynamical mass, computed using $W50'$ and a'_{HI} via eq. 3.

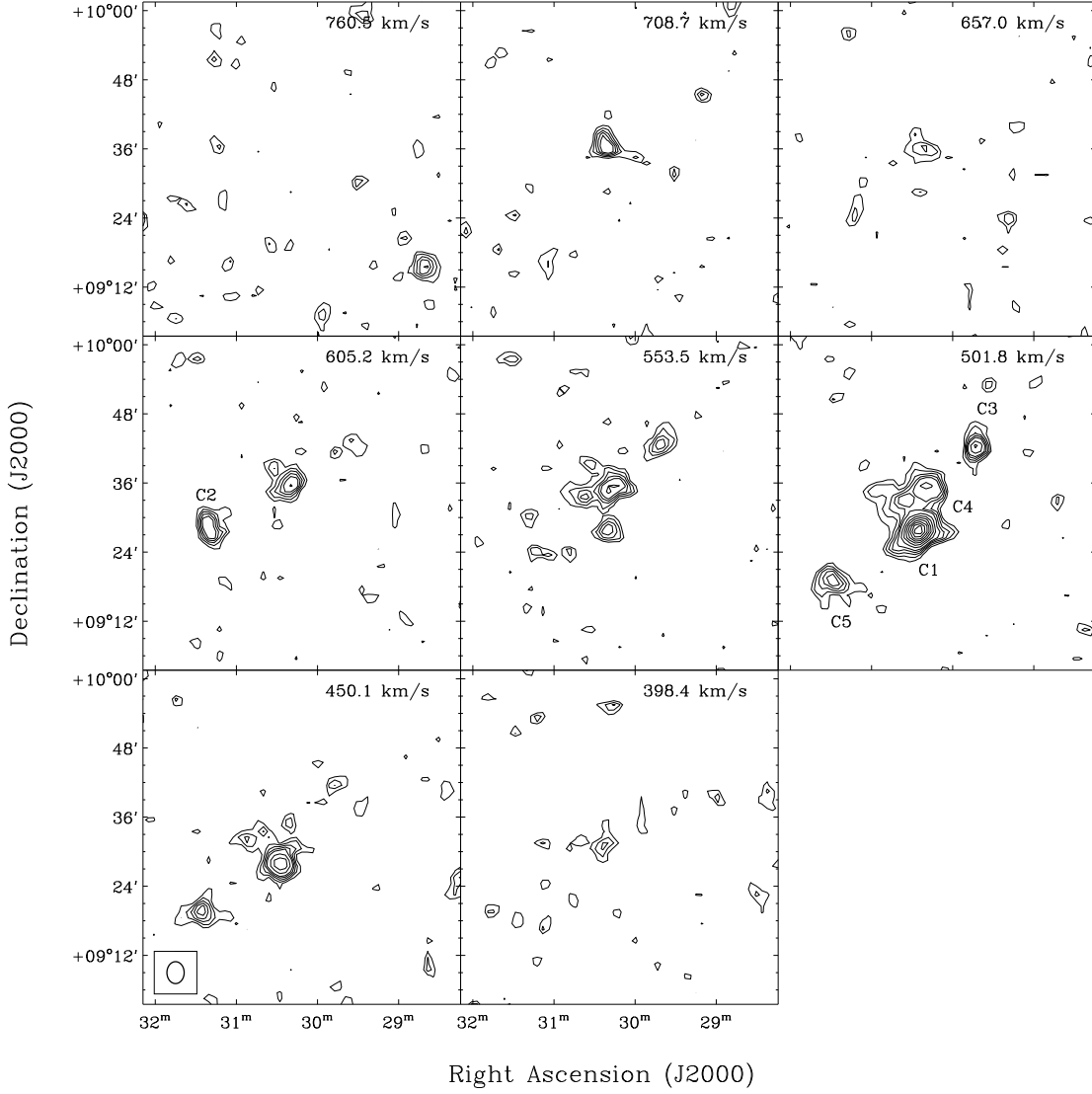


Fig. 1.— Channel maps of the cloud complex from 760 km s^{-1} to 400 km s^{-1} in the ALFALFA survey data. Contours are at (2, 3, 4, 5) and 6–26 mJy/beam in 2 mJy/beam intervals. The velocities indicated in the upper right corner represent the central channel velocity of the map. The maps are boxcar smoothed at the indicated velocities ± 5 channels (at $\sim 5 \text{ km s}^{-1}$ resolution). The five HI cloud detections are indicated as C1 through C5. The ellipse in the lower left indicates the ALFALFA beam size ($3'.3 \times 3'.8$).

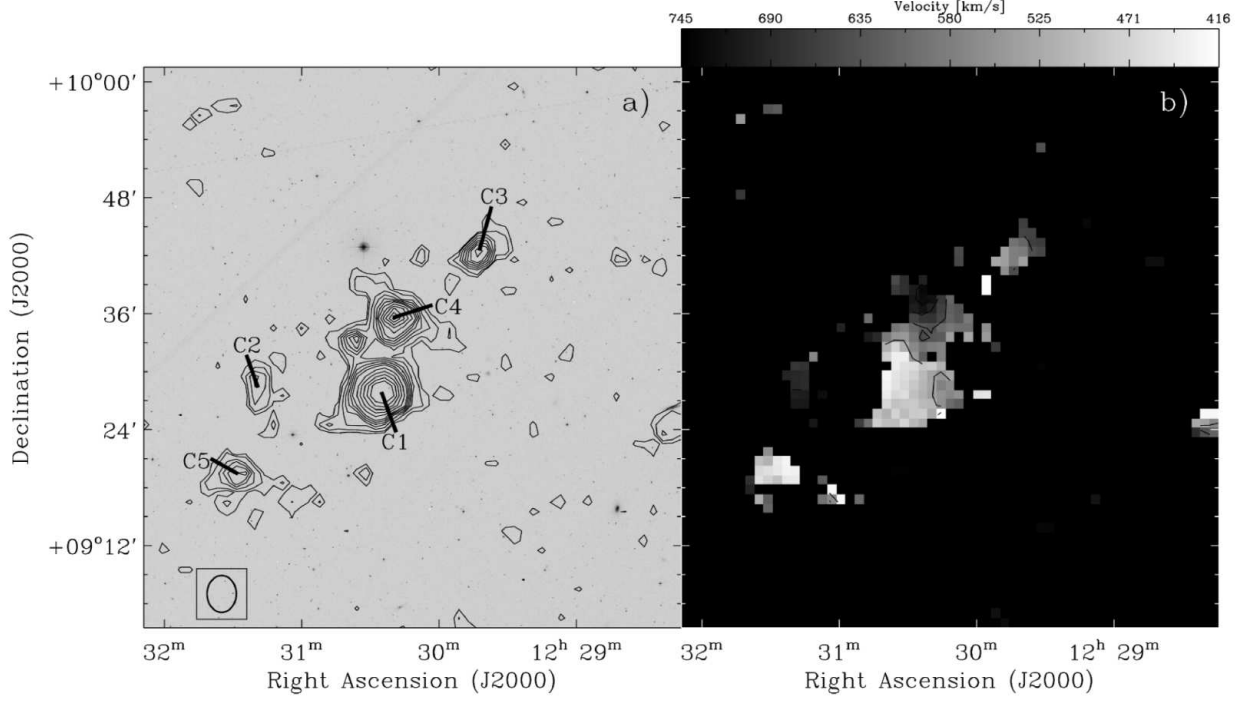


Fig. 2.— Global HI distribution and kinematics of the cloud complex. *a*) One square degree total intensity (zeroth moment) map of the cloud complex field. The cloud identifiers from Table 2 are indicated. The H I contours are 50, 100, 200, 300, 400, 500, 600, 800, 1000, 1200, 1400, 1600 mJy km s⁻¹ beam⁻¹. The background image is taken from the 2nd generation Digital Sky Survey B-band plates (Lasker *et al.* 1990). The ellipse in the lower left indicates the ALFALFA beam size (3'.3 × 3'.8). *b*) Intensity-weighted velocity (first moment) map. The linear scale bar ranges from 416-745 km s⁻¹. Contours indicate 450, 500, 550, 600, 650, 700 km s⁻¹. A color version of this figure is available in the electronic edition of the Journal.

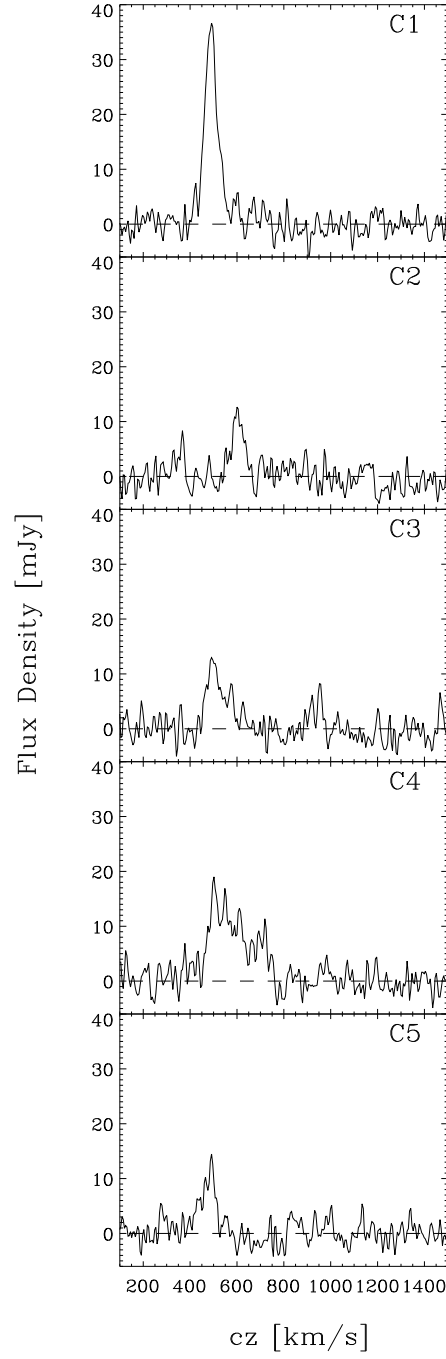


Fig. 3.— Integrated spectral profiles for C1-C5 at a resolution of $\delta V = 5.1 \text{ km s}^{-1}$. The average RMS across the five spectra is 2.13 mJy/channel.

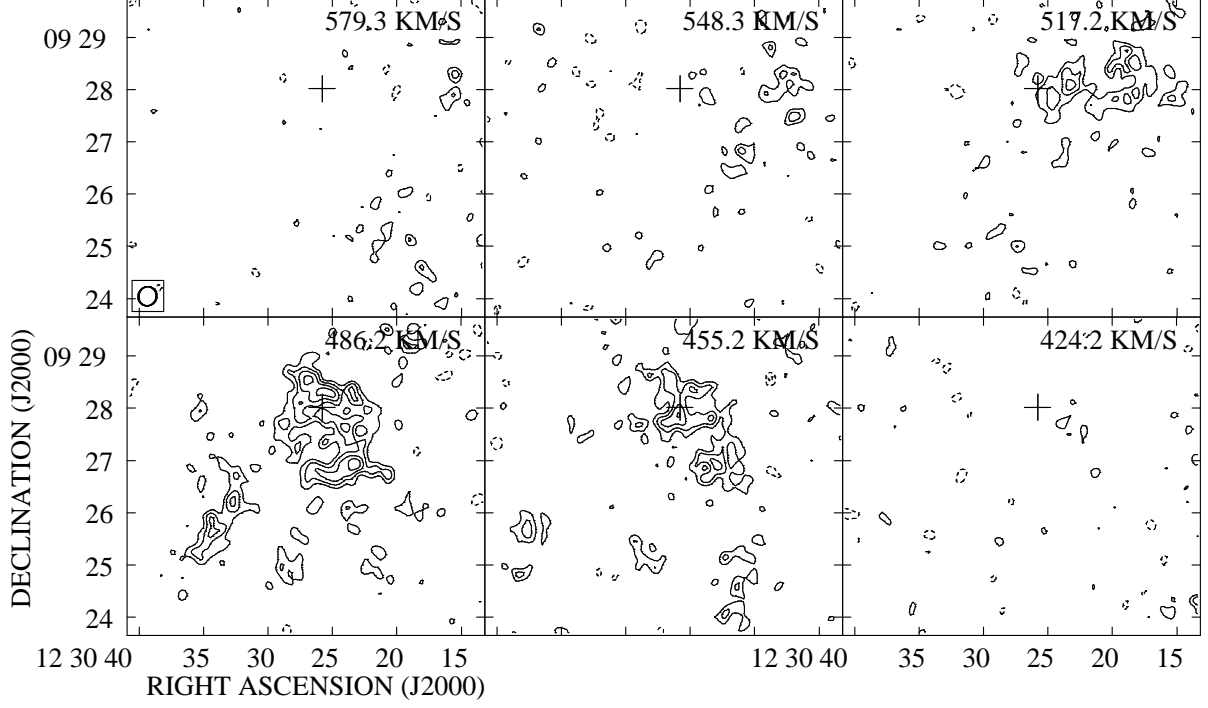


Fig. 4.— Naturally-weighted channel maps for C1 from the VLA observations. The plotted channels are independent ($\delta V' = 31 \text{ km s}^{-1}$). Contours are at $0.35 \times (-3, -2, 2 (2\sigma'_m), 3, 4, 5, 6) \text{ mJy/beam}$; negative contours are represented with dashed lines. The cross denotes the C1 centroid in the ALFALFA data (Table 2). The heliocentric radial velocity is in the upper right corner of each panel, and the synthesized beam is in the lower left corner of the first panel. A color version of this figure is available in the electronic edition of the Journal.

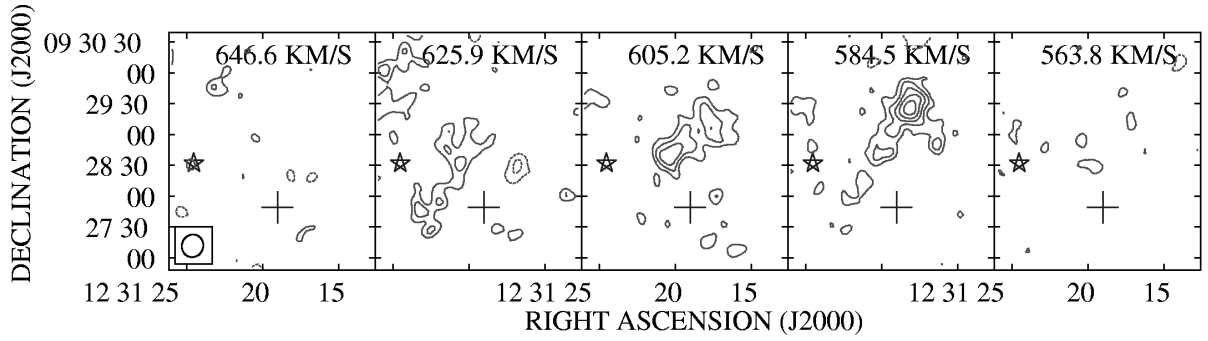


Fig. 5.— Naturally-weighted channel maps for C2 from the VLA observations. The plotted channels are independent ($\delta V' = 20.7 \text{ km s}^{-1}$). Contours are at $0.46 \times (-3, -2, 2 (2\sigma'_m), 3, 4, 5, 6) \text{ mJy/beam}$; negative contours are represented with dashed lines. The cross denotes the C2 centroid in the ALFALFA data (Table 2), and the star denotes the optical position of VCC 1357 (Binggeli *et al.* 1985). The heliocentric radial velocity is in the upper right corner of each panel, and the synthesized beam is in the lower left corner of the first panel.

A color version of this figure is available in the electronic edition of the Journal.

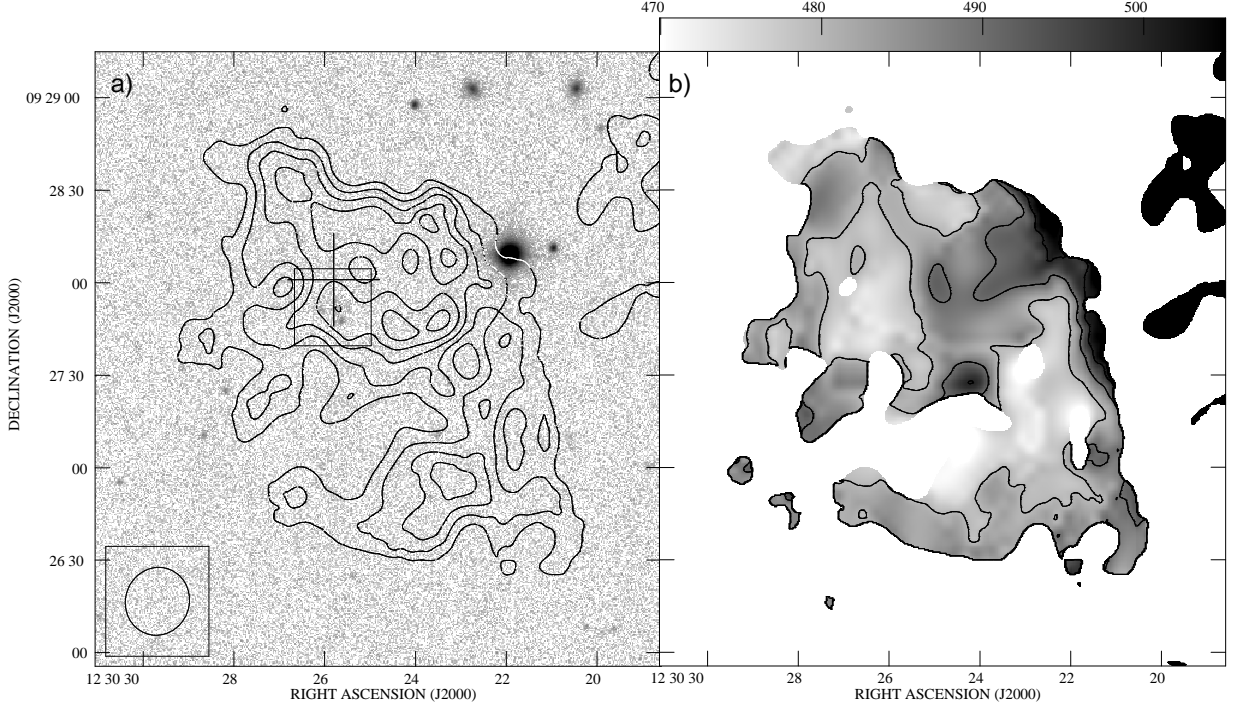


Fig. 6.— H I distribution and kinematics of C1 in the VLA data. *a*) Total intensity map of C1 (contours) superimposed on an SDSS *g* image (grayscale). Contours are at $N'_{HI} = 10^{20} \times (1, 1.5, 2, 2.5, 3) \text{ cm}^{-2}$, and the grayscale is plotted logarithmically. A very faint, uncatalogued source in the optical image is enclosed by the box. The cross indicates the centroid of the Arecibo detection for C1. The synthesized beam is in the lower left corner of the panel. *b*) Intensity-weighted velocity map of C1 in regions where $N'_{HI} \geq 10^{20} \text{ cm}^{-2}$. The grayscale spans 470–505 km s^{-1} on a linear scale, as indicated by the wedge at the top of the plot. Contours are at (480, 490, 500, 510) km s^{-1} . A color version of this figure is available in the electronic edition of the Journal.

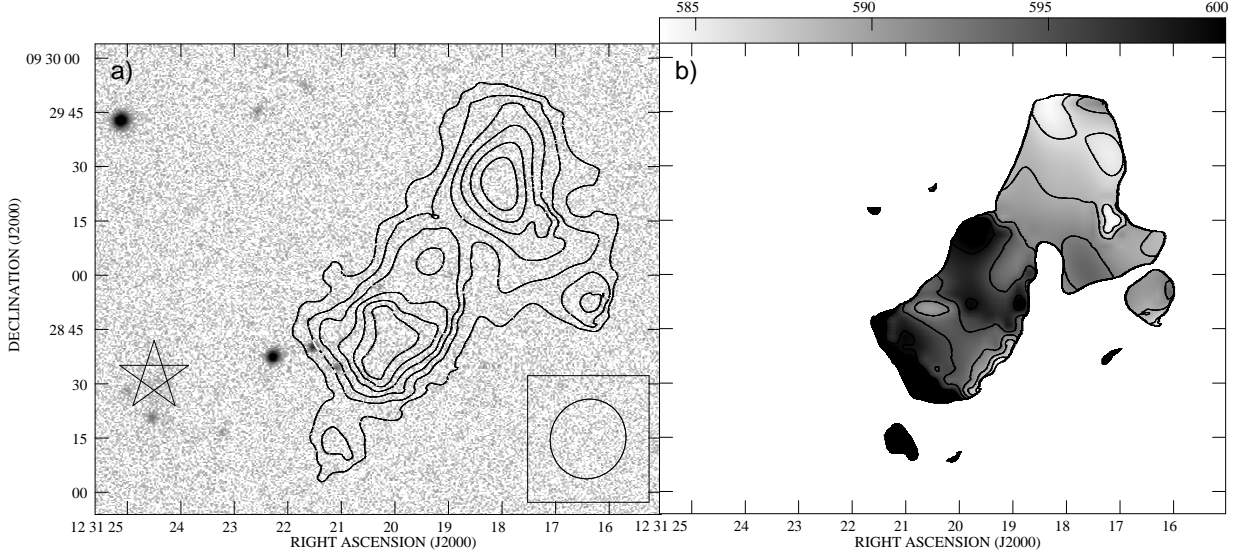


Fig. 7.— H I distribution and kinematics of C2 in the VLA data. *a*) Total intensity map of C2 (contours) superimposed on an SDSS *g* image (grayscale). Contours are at $N'_{HI} = 10^{20} \times (0.75, 1, 1.25, 1.5, 2, 2.25) \text{ cm}^{-2}$, and the grayscale is plotted logarithmically. The star indicates the location of VCC 1357 (Binggeli *et al.* 1985); it is just visible in the optical image. The synthesized beam is in the lower right corner of the panel. *b*) Intensity-weighted velocity map of C2 in regions where $N'_{HI} \geq 10^{20} \text{ cm}^{-2}$. The grayscale spans 585–600 km s^{-1} on a linear scale, as indicated by the wedge at the top of the plot. Contours are at (583, 586, 592, 595, 598) km s^{-1} . A color version of this figure is available in the electronic edition of the Journal.

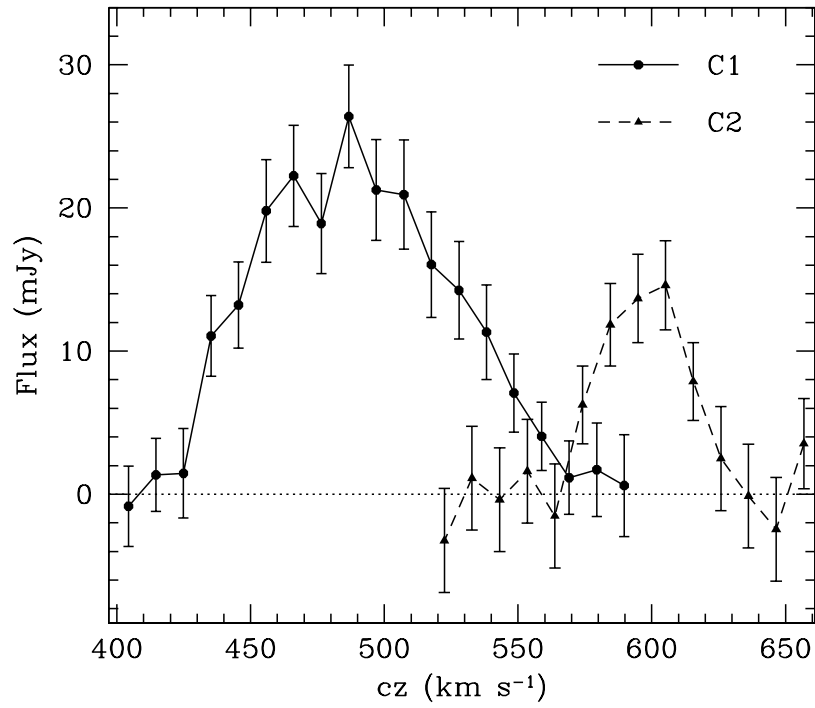


Fig. 8.— Integrated spectral profiles of C1 ($\delta V' = 31.0 \text{ km s}^{-1}$; solid lines and circles) and C2 ($\delta V' = 20.7 \text{ km s}^{-1}$; dashed lines and triangles) from the VLA observations. A color version of this figure is available in the electronic edition of the Journal.

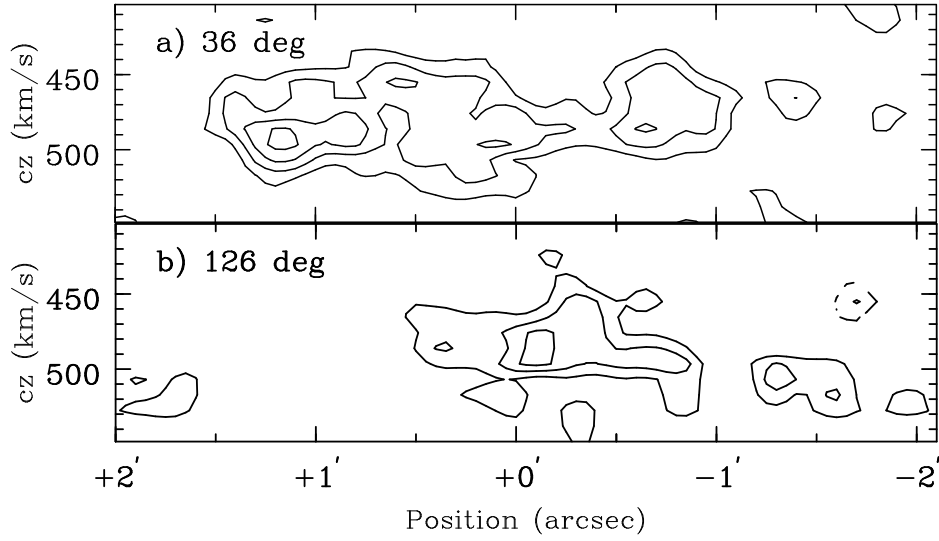


Fig. 9.— Position-velocity plot of the H I distribution in C1 along *a)* $PA'_{HI} = 36^\circ$, the position angle at which the maximum linear extent a'_{HI} was measured (see Table 4), *b)* the axis perpendicular to PA'_{HI} . In both panels, the position axis increases with increasing RA, and its origin corresponds to $\alpha' = 12^{\text{h}} 30^{\text{m}} 24.3^{\text{s}}$, $\delta' = +9^\circ 27' 41''$ (J2000). Contours are at $0.35 \times (-3, -2, 2 (2\sigma'_m), 3, 4, 5, 6)$ mJy/beam; negative contours are represented with dashed lines.

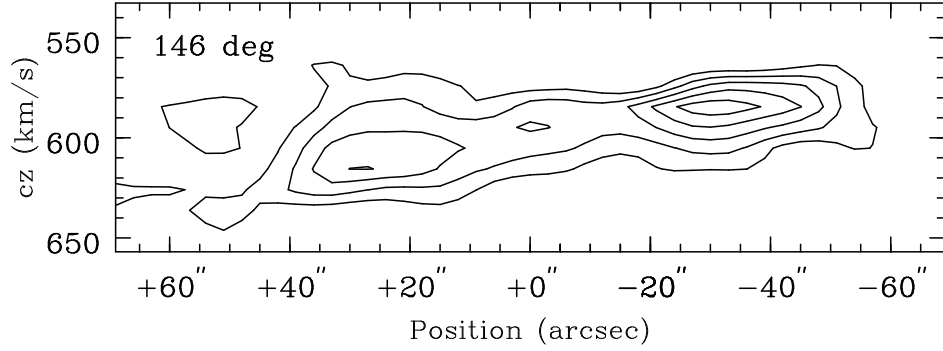


Fig. 10.— Position-velocity plot of the H I distribution in C2 along $PA'_{HI} = 146^\circ$, the position angle at which the maximum linear extent a'_{HI} was measured (see Table 4). The position axis increases with increasing RA, and its origin corresponds to $\alpha' = 12^{\text{h}} 31^{\text{m}} 19.2^{\text{s}}$, $\delta' = +9^\circ 29' 01''$ (J2000). Contours are at $0.46 \times (-3, -2, 2 (2\sigma'_m), 3, 4, 5, 6)$ mJy/beam; negative contours are represented with dashed lines.

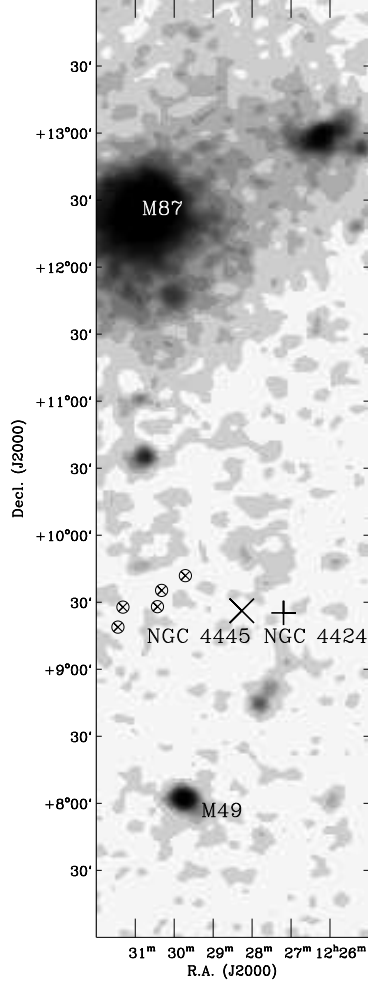


Fig. 11.— The environment of the H I cloud complex within the greater cluster area. The crossed circles indicate the five components of the complex discussed in this paper. The large plus(+) indicates the position of SBa galaxy NGC 4424 ($cz_{\odot} = 476 \text{ km s}^{-1}$). The large X indicates the position of Sab galaxy NGC 4445 ($cz_{\odot} = 354 \text{ km s}^{-1}$). The X-ray peaks are labeled indicating Virgo cluster galaxies M49 and M87 (Snowden *et al.* 1995). The symbols are not indicative of source sizes and are shown only for positional indication.

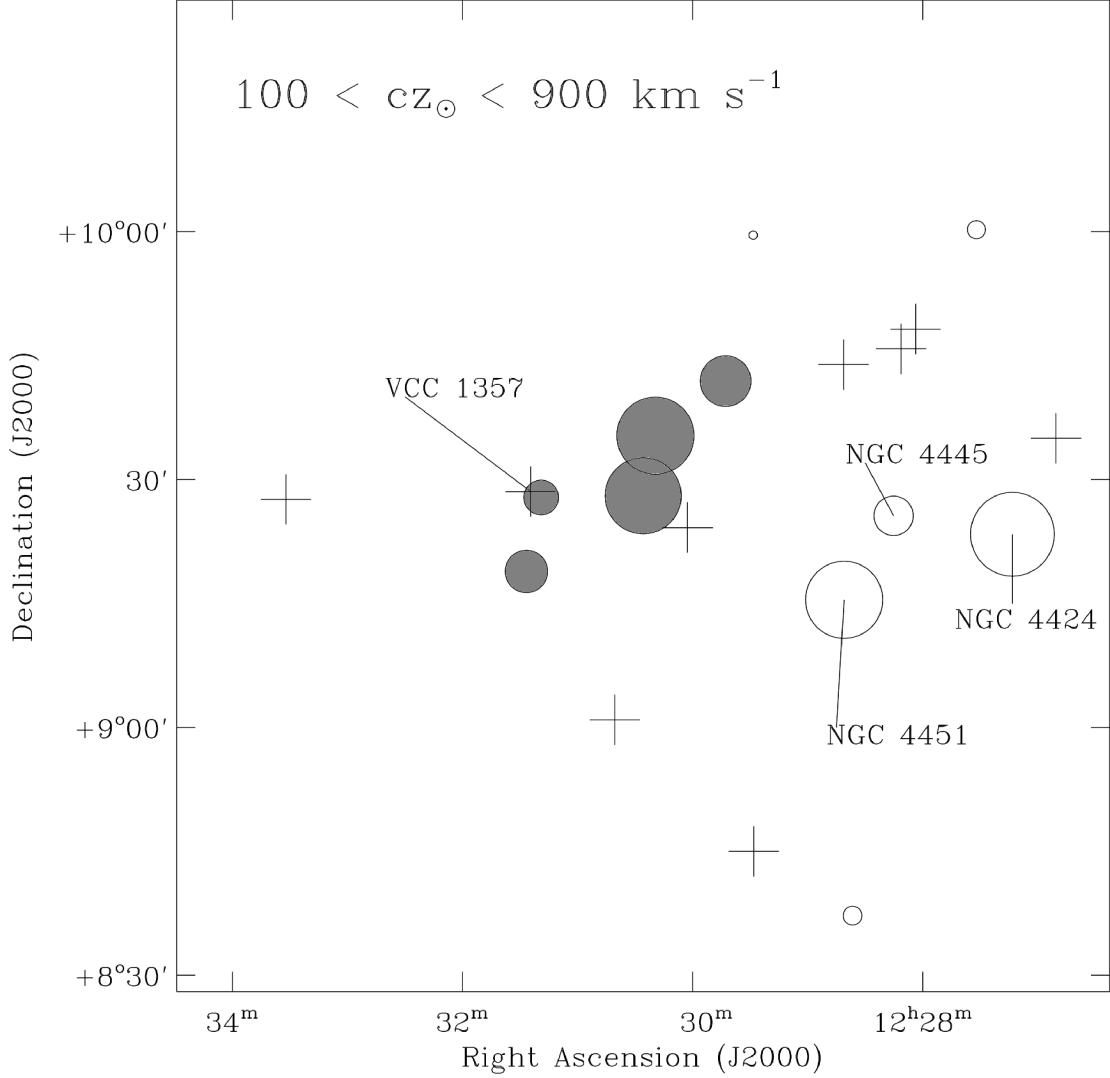


Fig. 12.— Galaxies in the vicinity of the cloud complex. The plot shows all objects with $100 < cz_{\odot} < 900 \text{ km s}^{-1}$ and within 1° of C1 listed in the Arecibo General Catalog. The cloud identifiers from Table 2 are indicated by the shaded circles. The crosses indicate objects without HI measurements from the ALFALFA survey. Objects with HI masses as measured from ALFALFA are shown as circles, with the circle radius indicative of the HI mass. The smallest circle indicates $\log_{10}(M_{\text{HI}}/M_{\odot})=7.30$ and the largest circle indicates $\log_{10}(M_{\text{HI}}/M_{\odot})=8.28$. Galaxies pertaining to the possible origin of the HI cloud complex are labeled for reference.

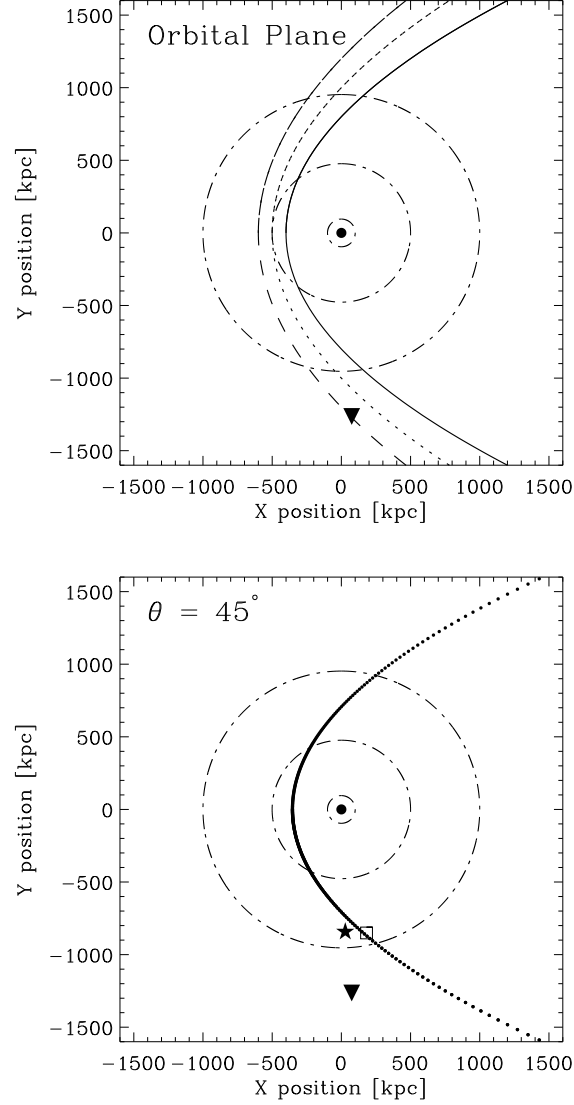


Fig. 13.— Simple schematic showing parabolic trajectories around the cluster. The axes are centered on the position of M87. The top plot shows parabolic trajectories in the orbital plane with $r_p=400$ (solid), 500 (dotted), and 600 (dashed) kpc. The position of M49 is shown as an inverted triangle. The dot-dashed concentric circles show radial distances of 100, 500 and 1000 kpc. The bottom plot shows the parabolic trajectory for $r_p=500$ kpc, corrected for an inclination of $\theta = 45^\circ$ to the line of sight. The positions of NGC 4445 (square) and HI cloud C1 (star) are also shown.

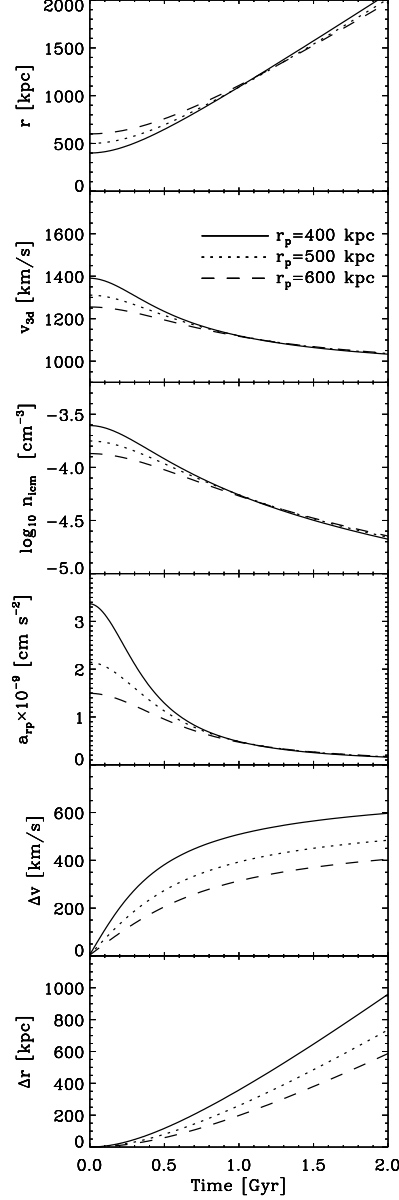


Fig. 14.— Results of a simple simulation of a galaxy moving in a parabolic orbit through the ICM. A cloud is detached from the galaxy at the pericenter distance, and experiences the dynamic effects due to ram pressure. The plotted parameters are not corrected for the inclination of the orbit to the line of sight. Three cases are shown for a pericenter distance of $r_p=400$ (solid), 500 (dotted), and 600 (dashed) kpc. Each plot is depicted as a function of time in gigayears since pericenter passage. The plots show (from top to bottom), r , the distance from the center of the cluster, v_{3d} , the velocity of the galaxy, $\log_{10} n_{icm}$, the base 10 logarithm of the ICM density as the galaxy moves through the cluster, a_{rp} , the acceleration on the detached HI cloud due to ram pressure, Δv , the velocity accumulated by the cloud due to acceleration by ram pressure, and Δr , the separation between the galaxy and cloud as they move in the parabolic orbit.

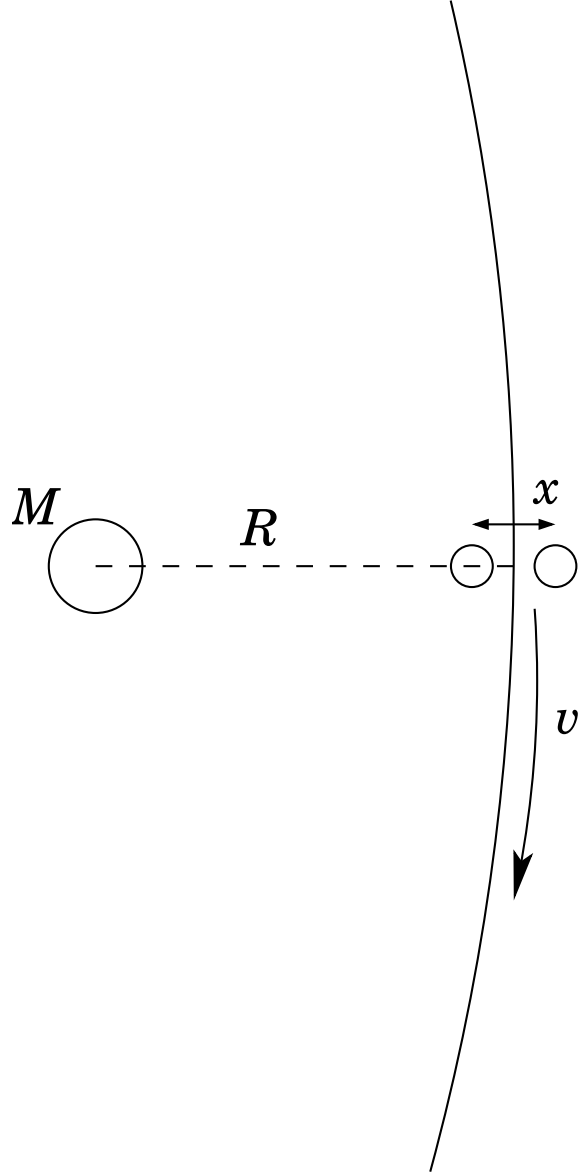


Fig. 15.— Schematic of an encounter of two clouds in a cluster. The clouds are separated by a distance x . The cloud complex model is located a distance R from the cluster core of mass M , moving at a velocity v relative to the cluster.